CM²

MAGAZINE

第 48 期

创刊词

海洋是生命的摇篮，是文明的纽带。地球上最早的生命诞生于海洋，海洋里的生命最终进化成了人类，人类的文化融合又通过海洋得以实现。人因海而兴。

人类对海洋的探索从未停止。从远古时代美丽的神话传说，到麦哲伦的全球航行，再到现代对大洋的科学钻探计划，海洋逐渐从人类敬畏崇拜幻想的精神寄托演变成可以开发利用与科学研究的客观存在。其中，上个世纪与太空探索同步发展的大洋科学钻探计划将人类对海洋的认知推向了崭新的纬度：深海（deep sea）与深时（deep time）。大洋钻探计划让人类知道，奔流不息的大海之下，埋藏的却是亿万年的地球历史。它们记录了地球板块的运动，从而使板块构造学说得到证实；它们记录了地球环境的演变，从而让古海洋学方兴未艾。

在探索海洋的悠久历史中，从大航海时代的导航，到大洋钻探计划中不可或缺的磁性地层学，磁学发挥了不可替代的作用。这不是偶然，因为从微观到宏观，磁性是最基本的物理属性之一，可以说，万物皆有磁性。基于课题组的学科背景和对海洋的理解，我们对海洋的探索以磁学为主要手段，海洋磁学中心因此而生。

海洋磁学中心，简称 CM^2，一为其全名"Centre for Marine Magnetism"的缩写，另者恰与爱因斯坦著名的质能方程 $E = MC^2$ 对称，借以表达我们对科学巨匠的敬仰和对科学的不懈追求。

然而科学从来不是单打独斗的产物。我们以磁学为研究海洋的主攻利器，但绝不仅限于磁学。凡与磁学相关的领域均是我们关注的重点。为了跟踪反映国内外地球科学特别是与磁学有关的地球科学领域的最新研究进展，海洋磁学中心特地主办 CM^2 Magazine，以期与各位地球科学工作者相互交流学习、合作共进！

"海洋孕育了生命，联通了世界，促进了发展"。 21 世纪是海洋科学的时代，由陆向海，让我们携手迈进中国海洋科学的黄金时代

目 录

研究进展

赵汉卿等，Geology：华北在寒武纪东、西方两大生物地理区生物交流中担纲的角色

根据特征三叶虫化石的古地理分布，寒武纪早期全球可以划分为东、西方两大生物地理区。其中，东区以东冈瓦纳大陆为主，特征三叶虫化石为莱德利基虫类（redlichiids），而西区主要包含劳伦（包括北美和格陵兰）、波罗的等大陆，以分布小油栉虫类（olenellids）三叶虫为特征。上述生物地理分区的产生，有一部分原因被解释为是寒武纪早期（~520 Ma）冈瓦纳和劳伦大陆分离形成古大西洋（Iapetus Ocean）的结果。然而，随着古大西洋盆地的扩张，在寒武纪中、晚期，生物地理分区的界线却逐渐模糊。对于两大生物地理区的生物是在什么时间、通过怎样的方式进行交流的，仍然是早期生物演化和生物古地理学研究中的未解谜题。以往的生物古地理研究基于莱德利基虫类和小壳化石等证据，认为华北地块与东冈瓦纳大陆在寒武纪早期具有较强的亲缘关系。而最近的古生物学研究在华北寒武系地层中发现了 *Sidneyia* 和 *Cambroraster* 等典型的布尔吉斯页岩型化石，是这两种节肢动物化石在劳伦以外大陆的首次发现。这表明在寒武纪中期，华北陆块可能与劳伦大陆也存在生物古地理方面的关联性。

针对上述科学问题，中国地质大学（北京）博士研究生赵汉卿在张世红教授的指导下，在苏北和鲁西两地区寒武系乌溜阶（~505 Ma）徐庄组地层中获得了新的古地磁数据，通过与前人在华北其它地区报道的徐庄组结果进行综合，计算出华北~505 Ma 的可靠古地磁极（31.8 °S, 140.4 °E, $A_{95} = 5.3°$）。该磁极通过了区域一致性检验，并具有双极性。古地磁结果表明：在寒武纪中期华北应该位于北纬20°附近。综合古生物学和大地构造学等方面的证据，他们的研究认为：在寒武纪中期华北可能处于古太平洋内，并位于劳伦和东冈瓦纳大陆之间。最晚自

~520 Ma 开始，在古太平洋边缘出现了大量的岩浆弧，并形成一系列的构造古地理群岛。在低纬度西向洋流的作用下，华北连同这些环太平洋群岛，可能大大促进了寒武纪中、晚期东、西方两大生物地理区的生物交流。
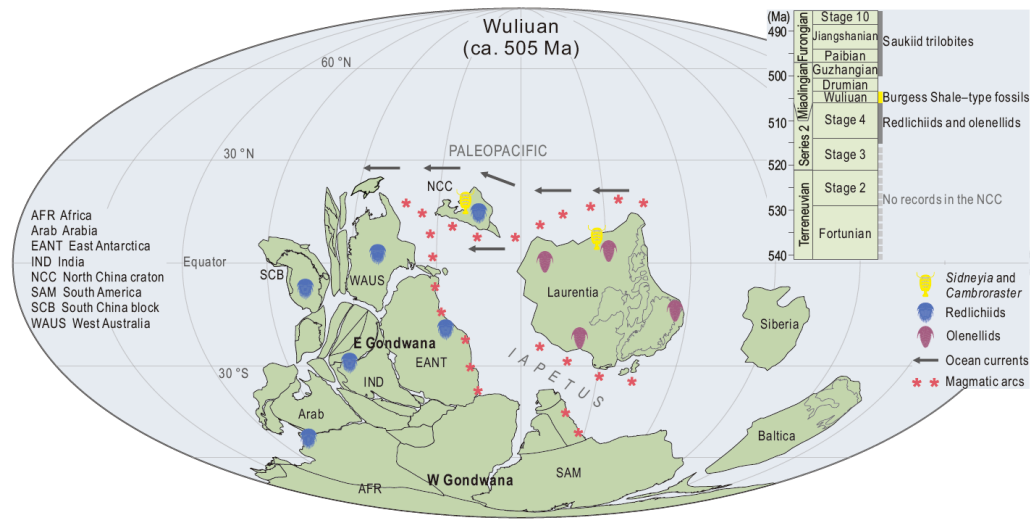
作者简介：赵汉卿，博士，主要从事构造古地磁学和磁性地层学研究，2020年博士毕业于中国地质大学（北京），师从张世红教授。现在中国地质大学(北京)地球科学与资源学院从事博士后研究工作。

岩石磁学演绎

第 38 章　非磁性技术

凭借测量和数据分析方法的进步，环境磁学正日渐成为一门精细的定量化学科。这些方法中，首先要提到低温测量手段。像热磁方法一样，低温下可以测量剩磁，高场磁化强度以及交变磁化率，并且样品可免受高温（>100 °C）加热引起的矿物变化。低温测量的方法特别适合研究纳米级的铁氧化物的磁学性质，比如超顺磁性和粒径效应引起的磁矩增强。

其次是同步辐射 X 射线吸收谱技术。同步辐射发射的 X 光源在研究原子尺度的精细结构上有重要的应用，比如，电子状态，原子配位结构，固体结构，固体的氧化状态和磁性。这些应用并不像传统的 XRD 技术那样依赖样品的物理性质，比如同步辐射 X 射线对结晶程度不同的纳米颗粒同样适用。而且同步辐射技术的测量非常迅速，因此可以测量模拟自然界氧化还原反应的化学实验。这些优势可以很好地辅助环境磁学研究，更深刻地理解自然过程。

同步辐射装置是同步加速器中的电子储存环。带电粒子作加速运动时都会产生电磁辐射，所以当加速器中的电子束被注入插入元件时，电子运动方向被弯转磁铁或波荡器改变并释放出包括 X 射线在内的辐射光源。辐射光源的性质决定于电子储存环的能量，X 射线的能量从几百电子伏至上万电子伏不等。同步辐射沿着储存环管壁切向的引出口进入光束线路。光束线路中配有不同的光学装置，最重要的装置是单色器，起到分选入射光源能量范围的作用。光源经过能量分选、分光和聚焦后，进入与光束线末端相连的实验站。实验站内包

括探测器、数据采集系统和控制系统等设备，可满足不同的测量需求。

同步辐射 X 射线吸收光谱可以测量样品对具有不同入射能量的 X 射线的吸收系数。随着能量的升高，吸收系数出现多次非连续性突变，这些吸收光谱上突变处称为吸收限。吸收限对应的能量等于被激发的内层电子的束缚能，并且根据被激发的内层电子的层位命名吸收限。K 吸收限对应的内层电子为 1s 层电子，L1 吸收限对应 2s 层电子，L2,3 吸收限对应 2p 层电子。X 射线吸收光谱(XAS)上可以明显区分开三个区域。吸收限之前的区域(pre-edge region)反映了吸收原子的氧化状态和配位状态，吸收限附近的区域称为 X 射线吸收近限谱(XANES)，是由吸收原子的邻近原子对出射光电子的背散射引起的，可作为一个特征来与标准样品进行对比 [Dräger et al., 1988; Bajt et al., 1994; Fredrickson et al., 2000; Mikhailova et al., 2005]。扩展 X 射线吸收谱(EXAFS)能够反映吸收原子与相邻原子间的距离，以及相邻原子的数量和类型。Guyodo et al. [2006b] 将该方法应用到排列不良(poorly-ordered)的不同粒径的六线水铁矿的研究上，这些水铁矿的低温磁性存在差异，而根据其在铁的 K 吸收限的扩展 X 射线吸收谱，可以判断这些矿物的 Fe-O 和 Fe-Fe 键的平均距离相同，意味着它们的短程排列相似。由于这些样品短程与长程排列的相似性，研究者将样品的低温磁性的差异归结为由粒径引起而并非矿物结构的差异导致。借助 EXAFS 的研究还发现水铁矿中有 20-30% 的 Fe^{3+} 位于四面体结构中，证实了之前的假设 [e.g., Michel et al., 2007, 2010]，但也有不同的研究结果 [e.g., Drits et al., 1993; Jambor and Dutrizac, 1998; Manceau, 2009, 2011]。对水铁矿在铁的 K-和 L2,3 吸收限的 X 射线磁性圆二色(x-ray magnetic circular dichroism, XMCD) 的测量（图

4)[Guyodo et al., 2012] 表明六线水铁矿晶格的四面体结构中有大量的 Fe^{3+}，与 Maillot et al.[2011] 的 EXAFS 结果一致。

XMCD可以获得特定元素的轨道磁矩和自旋磁矩，因此适合研究微观相互作用、粒径效应等引起的铁磁性材料磁矩微小的变化。铁磁性材料中具有未配对的电子自旋，即向上自旋与向下自旋的数目不等，这导致其对入射X射线的左右旋圆偏振光的吸收系数不相同，这就是XMCD [Schütz et al., 1987]。实验表明，在外加磁场中（强度最大可达几个特斯拉）依靠左圆偏振和右圆偏振两种X光源获得两条吸收谱，可以用来导出XMCD谱。Brice-Profeta et al. [2005] 使用XMCD研究了不同粒径和表面镀膜的磁赤铁矿，他们发现L2,3 吸收限处，晶格中八面体和四面体内的铁原子是矿物宏观磁性的载体。他们发现三类样品中四面体与八面体中的铁元素占有率的比值相同，而小粒径和表面镀膜的纳米颗粒的八面体结构中的 Fe^{3+} 自旋排列比较无序。这一研究结果支持了纳米磁赤铁矿的内核/外壳模式的假设，这一模式认为纳米颗粒表面的自旋与内部原子的自旋交换相互作用低于内部自旋间的作用强度。

Carvallo et al. [2008] 对冷却到 200 K的纳米磁铁矿测量了铁L2,3 吸收限的XMCD谱。实验结果表明生物成因的磁铁矿中 Fe^{2+} 含量比无机成因的磁铁矿更丰富，这就能解释生物成因的磁铁矿具有更完善的结晶程度与标准的化学计量的原因。Lam et al. [2010] 使用扫描透射X射线显微技术(STXM)和XMCD研究了海洋类弧菌MV-1（一种在海水中发现的趋磁细菌）体内的磁小体（趋磁细菌体内被细胞膜包裹的磁铁矿或胶黄铁矿），发现磁小体内确有过量的 Fe^{2+}。

综上所述，使用同步辐射技术可以对样品做空间尺度上非常精细的研究，并且不需要样品具有周期性的结构。因此该方法对于低结晶度的矿物和纳米颗

粒这些环境研究非常关注的对象也适用,对这些样品表面性质的研究可以反映出许多环境信息。另外,通过这类技术可以深入理解铁氧化物原子尺度的磁性特征,从而有助于建立更真实的模型来理解样品宏观磁性与环境变化之间的关系。比如,弄清结晶不发育(由于反应速度过快等因素导致)的晶体表面原子的排列将有助于模拟重金属吸收,矿物分解/沉淀,或者氧化还原反应过程[e.g., Boily et al., 2001; Rustad and Felmy, 2005; Casey and Rustad, 2007]。这些优势使得同步辐射技术将在环境磁学领域得到更多的重视和应用。

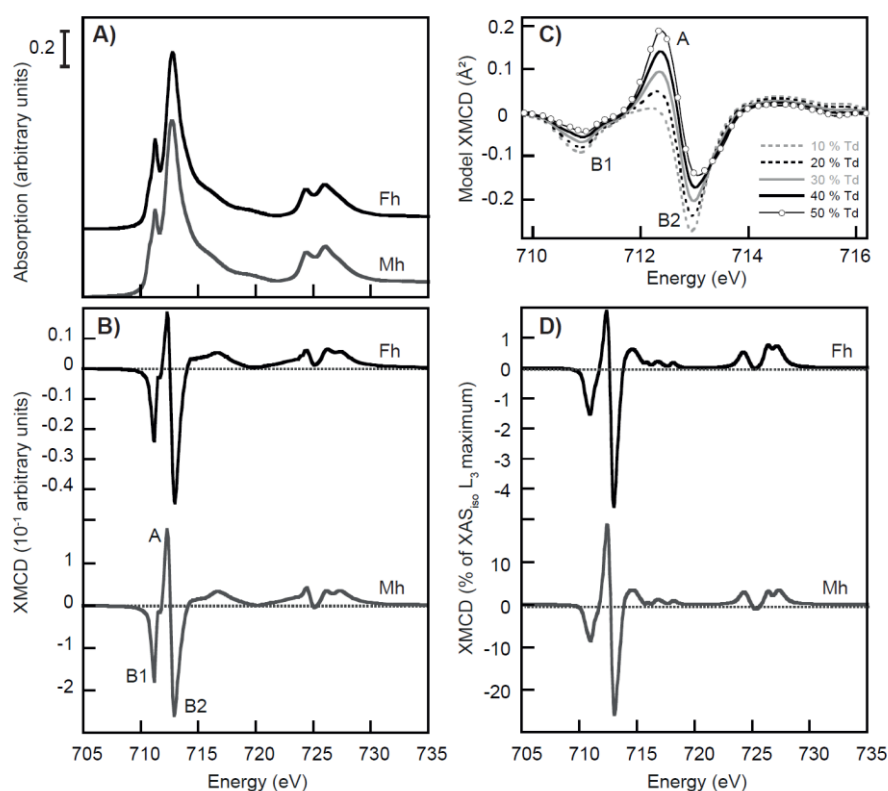图 1. (A) 合成6线水铁矿(Fh)和磁赤铁矿(Mh)的$L_{2,3}$边各向同性的X射线吸收谱(XAS),温度为15 K,瑞士光源(参考 *Guyodo et al.* [2012]). (B) Fh和Mh对应的XMCD谱,在6 T磁场下左右循环极化的XAS的差. 数据是多次实验的平均值,根据前人的配位场多次谱理论计算[*Brice-Profeta et al.*, 2005],由四面体内的铁(Fe$_{Td}$)引起的正向峰值标记为A,而另外两个由八面体内的铁(Fe$_{Oh}$)引起的负向峰值标记为B1和B2. Fh的XMCD谱形状与Mh的类似,这表明Fh中含有大量的Fe$_{Td}$. (C) Fe$_{Td}$的含量变化对利用配位场多次谱理论计算的XMCD形状的影

响，这表明A和B2峰对Fe_{Td}的含量最为敏感；(D) Fe_{Td}的含量分别为28%和37.5%的Fh和Mh的XMCD谱.

文献速递

1. 2900 年以来北大西洋海表温度年际变化

翻译人：仲义 zhongy@sustech.edu.cn

摘要：由于人类因素造成的全球变暖可以被自然气候波动放大或减弱，特别是那些涉及到北大西洋海洋表面温度（SSTs）的变化在多年尺度上（大西洋年代际变化，Atlantic multidecadal variability，AMV）。由于 AMV 在仪器测试记录上非常短，因此 AMV 的长期变化行为是未知的，但是北大西洋以外地区的气候遥相关可以为从其他地区的高分辨率记录重建提供了条件。从埃尔斯米尔岛沉积记录中年际 Ti 含量变化表明，通过大气环流异常的变化该记录受到 AMV 的控制。这种高北极指标和其他高分辨率大西洋海表温度指标之间的显著相关系表明，它可以直接记录到大西洋中的年际变化。我们的记录提供了过去 3000 年 AMV 重建方面前所未有的时间精度，结果显示在北大西洋 SST 在 1400-1800 年前温度最低，而当前的 SST 温度已达到 2900 年以来的最高峰。

ABSTRACT: Global warming due to anthropogenic factors can be amplified or dampened by natural climate oscillations, especially those involving sea surface temperatures (SSTs) in the North Atlantic which vary on a multidecadal scale (Atlantic multidecadal variability, AMV). Because the instrumental record of AMV is short, long-term behavior of AMV is unknown, but climatic teleconnections to regions beyond the North Atlantic offer the prospect of reconstructing AMV from high-resolution records elsewhere. Annually resolved titanium from an annually laminated sedimentary record from Ellesmere Island, Canada, shows that the record is strongly influenced by AMV via atmospheric circulation anomalies. Significant correlations between this High-Arctic proxy and other highly resolved Atlantic SST proxies demonstrate that it shares the multidecadal variability seen in the Atlantic. Our record provides a reconstruction of AMV for the past ~3

millennia at an unprecedented time resolution, indicating North Atlantic SSTs were coldest from ∼1400–1800 CE, while current SSTs are the warmest in the past ∼2,900 y.
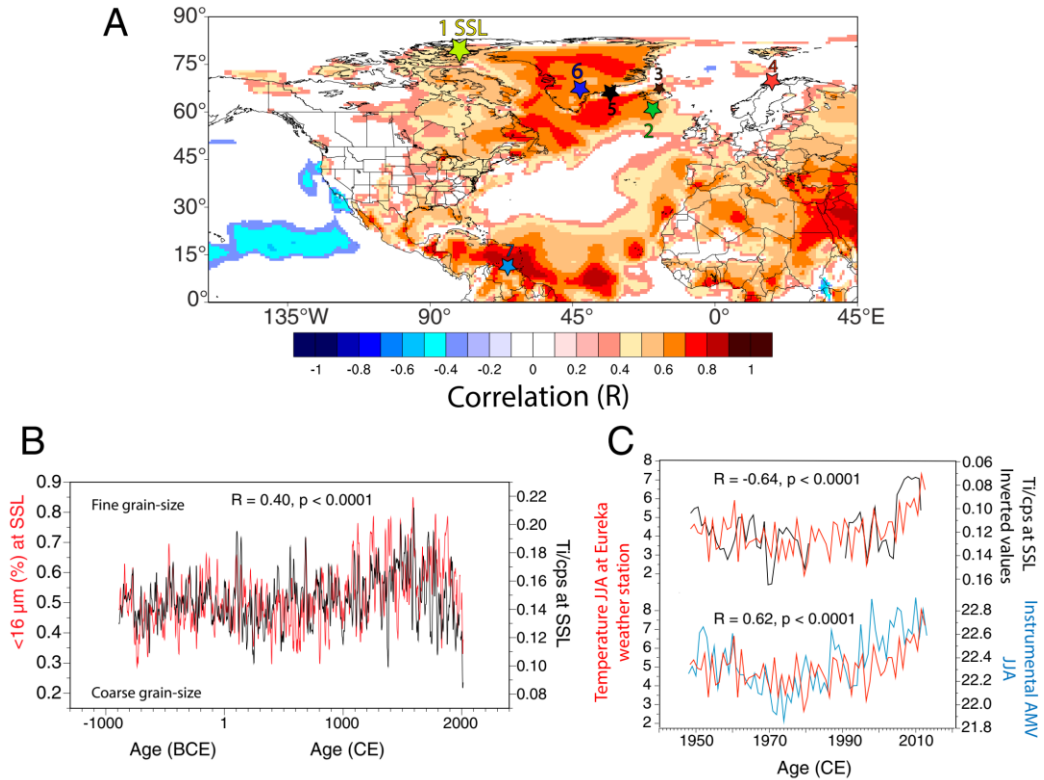

Figure 1. AMV during summer in the North Atlantic. (A) Spatial correlation between instrumental AMV and 2-m temperature from ERA-Interim (15) from 1979 to 2019. The numbering 1–7 corresponds to sites referred to in the text: SSL (1), Rapid-17–5P (2), A. islandica from bivalve shells (3), BWTs at Malagen (4), SIC in southeast Greenland (5), DYE-3 ice record (6), and G. bulloides abundance at Cariaco Basin (7). Map created using University of Maine Climate Reanalyzer, https://climatereanalyzer.org/. (B) Annually fine grain size (% <16 μm) (16) compared to Ti at SSL (cps: counts per second) over the past 2,900 y. Data are filtered by an 11-y Gaussian filter. (C, Upper) Comparison between SSL Ti (inverted values) and instrumental temperature (JJA, 3-y running mean) at Eureka weather station located 60 km northeast of SSL. (C, Lower) Same as Upper, but using the unsmoothed (and unaltered) instrumental AMV from Kaplan SST (17). Note that a turbidite dated to 1990 eroded 9 varves (16).
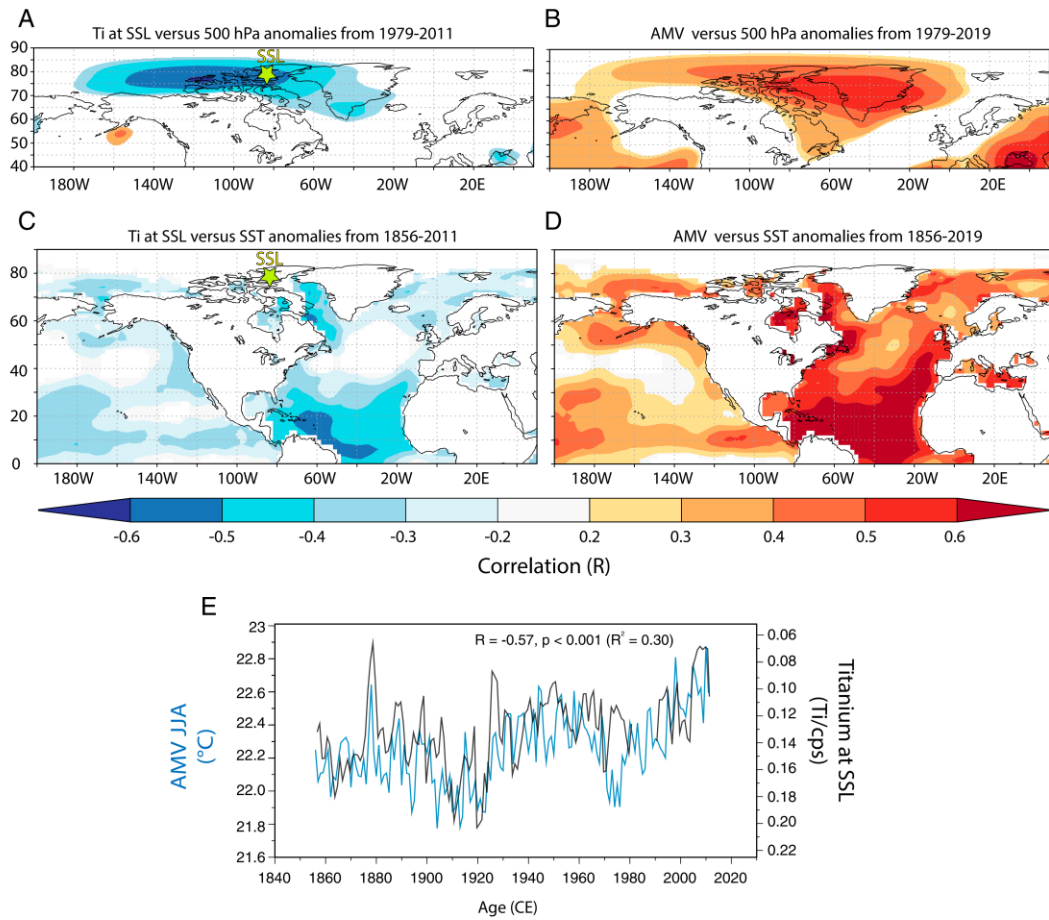
Figure 2. Ti variability at SSL and its relationship with instrumental AMV. (A) Map correlation between Ti variability and atmospheric pressure at 500 hPa from ERA-Interim (15) during summer (JJA) from 1979 to 2011. (B) Same as A but for the instrumental AMV (17) during summer (JJA) from 1979 to 2019. (C and D) Same as A and B but Ti at SSL (1856–2011) and instrumental AMV (1856–2019) correlated to SST anomalies from the Extended Reconstructed Sea Surface Temperature, version 5 (28). (E) Comparison between Ti at SSL (inverted values) and the instrumental summer (JJA) AMV over the instrumental period 1856–2011 (17). Yellow star (A and C) denotes the location of SSL record.
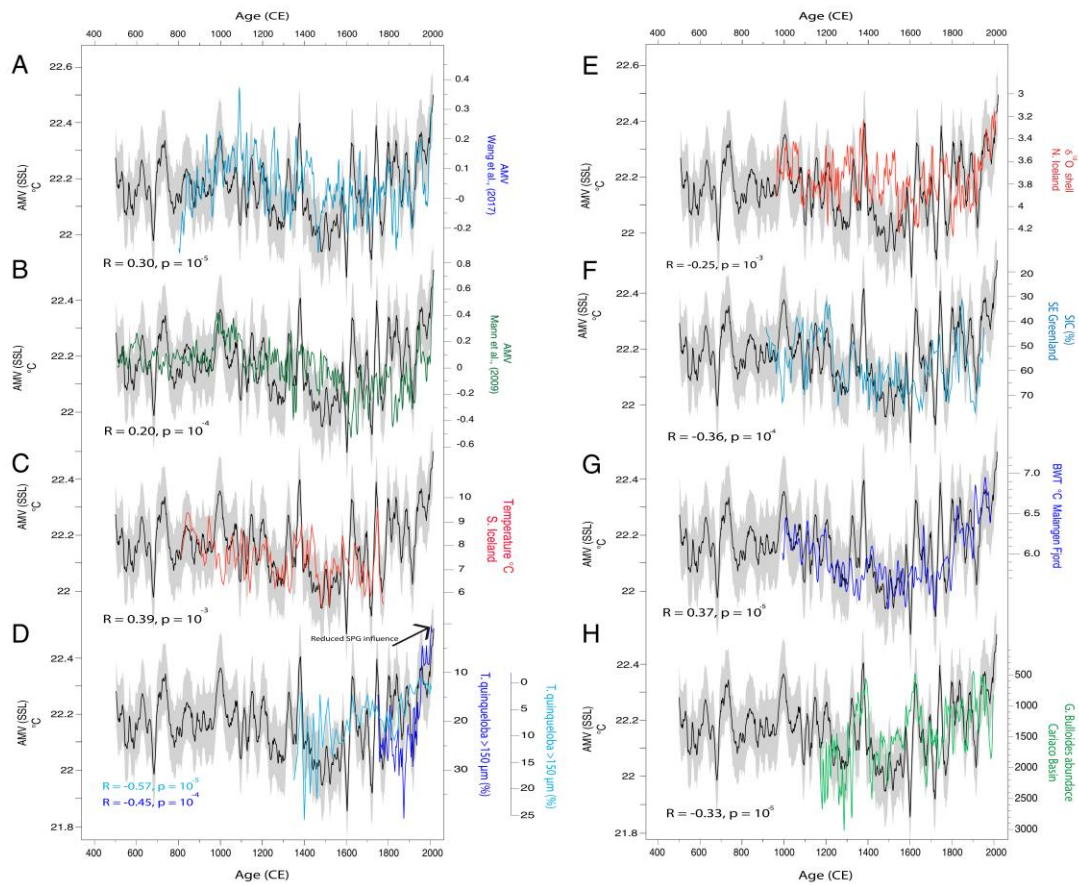
10

Figure 3. SSL record and its relationship with subdecadal Atlantic SST. (A) AMV based on the Ti record from SSL (AMVSSL) compared to reconstructed AMV (12). (B to H) Same as A but AMVSSL compared to AMV from Mann et al. (B) (13), ocean temperature south of Iceland from core Rapid-17–5P (C) (31), T. quinqueloba (light blue) from core EN539-MC14-A and T. quinqueloba (dark blue) from core MC16-A (D) (32), the δ¹⁸O from shells of the long-lived marine bivalve A. islandica (E) (33), the SIC off SE Greenland (F) (34), the BWT at Malangen Fjord (G) (35); and G. bulloides abundance from Cariaco Basin (H) (36). In D, SPG stands for subpolar gyre. Shaded gray regions represent the 95% confidence intervals on the reconstructed AMVSSL, based on uncertainty estimates (Methods).

2. 白垩纪生物大灭绝后大型底栖动物快速多样化与稳定

翻译人：蒋晓东 jiangxd@sustech.edu.cn

摘要：先前在墨西哥尤卡坦半岛希克苏鲁伯陨石坑（IODP/ICDP M0077）足迹化石分析，揭示白垩纪末生物大灭绝后造迹生物群落（tracemaker）快速恢复。本研究发现生物的完全恢复也是快速的，通过建立 700 ky 的群落分层，观察到生物恢复的几个阶段具有显著的稳定性与多样性。分层的最后阶段观察到动藻痕迹，管枝迹和漫游迹，均归属于藻痕迹类。多样性的增加同时伴随着更大丰度，更大形态更复杂的堆叠结构。如此快速的生物恢复表明在陨石撞击盆地适宜的古环境快速重建，确保生物栖息之地。与二叠纪末生物大灭绝相比，这次生物恢复显得更快。快速恢复暗示大型底栖生物在白垩纪大灭绝事件后的演化意义。本研究有助于理解白垩纪事件后生物群落如何回复以及这次事件与其他大灭绝事件的不同之处。

ABSTRACT: Previous ichnological analysis at the Chicxulub impact crater, Yucatán Peninsula, México (International Ocean Discovery Program [IODP]/International Continental Scientific Drilling Program [ICDP] Site M0077), showed a surprisingly rapid initial tracemaker community recovery after the end-Cretaceous (Cretaceous-Paleogene [K-Pg]) mass extinction event. Here, we found that full recovery was also rapid, with the establishment of a well-developed tiered community within ~700 k.y. Several stages of recovery were observed, with distinct phases of stabilization and diversification, ending in the development of a trace fossil assemblage mainly consisting of abundant *Zoophycos, Chondrites*, and *Planolites*, assigned to the *Zoophycos ichnofacies*. The increase in diversity is associated with higher abundance, larger forms, and a deeper and more complex tiering structure. Such rapid recovery suggests that favorable paleoenvironmental conditions were quickly reestablished within the impact basin, enabling colonization of the substrate. Comparison with the end-Permian extinction reveals similarities

during recovery, yet postextinction recovery was significantly faster after the K-Pg event. The rapid recovery has significant implications for the evolution of macrobenthic biota after the K-Pg event. Our results have relevance in understanding how communities recovered after the K-Pg impact and how this event differed from other mass extinction events.

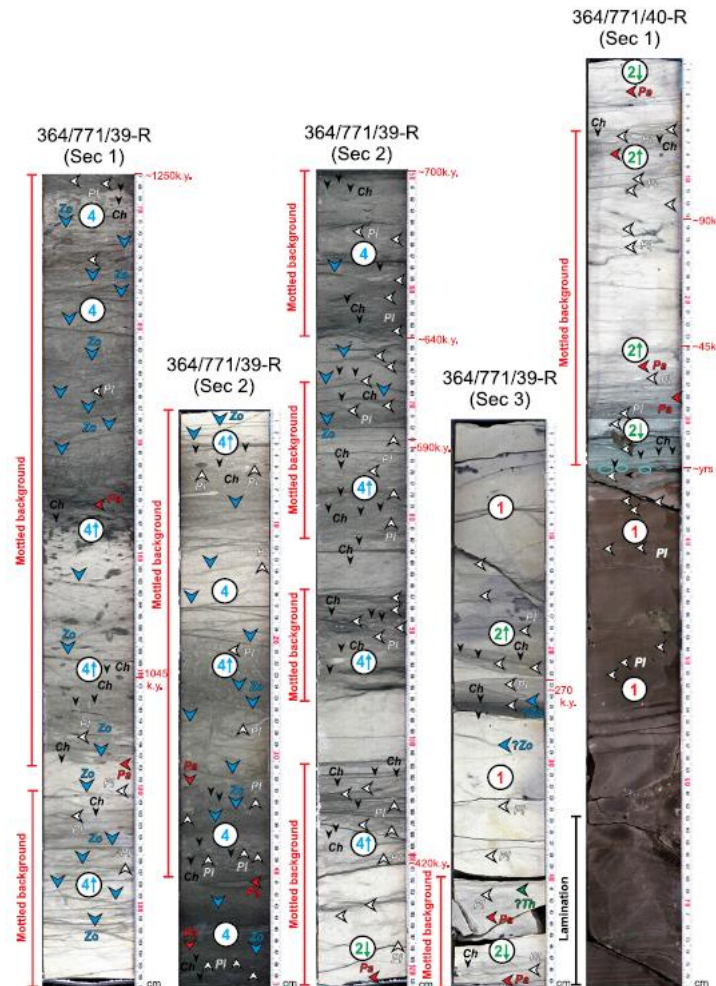Figure 1. Sedimentological and ichnological features through the studied cores, from the Chicxulub impact crater, Yucatán Peninsula, México (International Ocean Discovery Program [IODP]/International Continental Scientific Drilling Program [ICDP] Site M0077. *Ch—Chondrites* (black arrows); *Pa—Palaeophycus* (red arrows); *Pl—Planolites* (yellow arrows); *Zo—Zoophycos* (blue arrows); BI—bioturbation index (0–4).

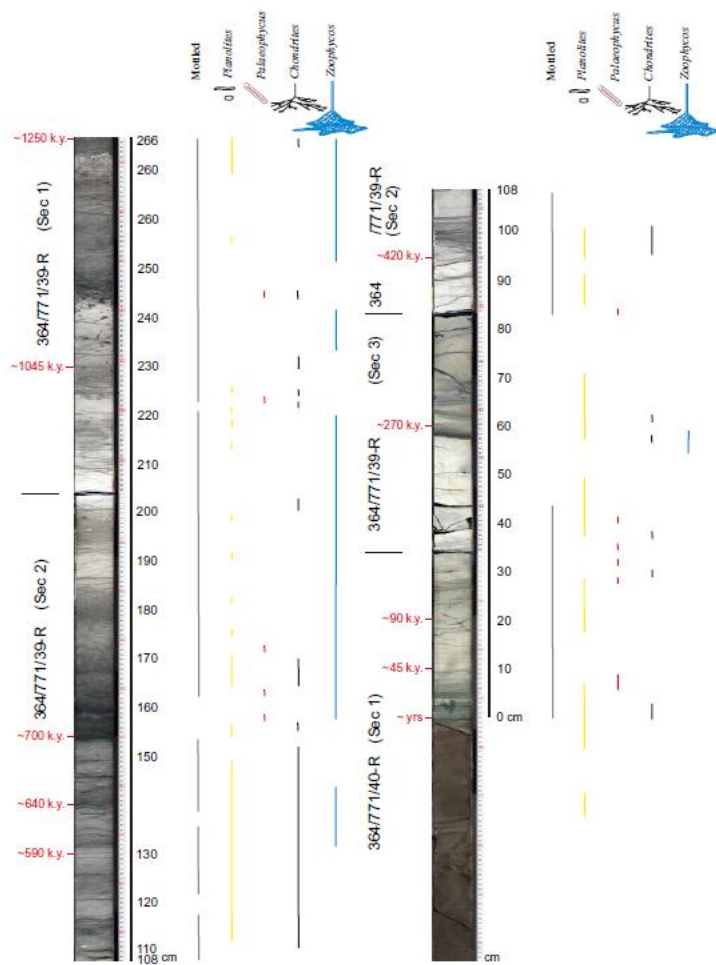Figure 2. Distribution of ichnotaxa in cores from International Ocean Discovery Program (IODP)/ International Continental Scientific Drilling Program (ICDP) Site M0077, showing distance from the top of the Transitional Unit and corresponding age.
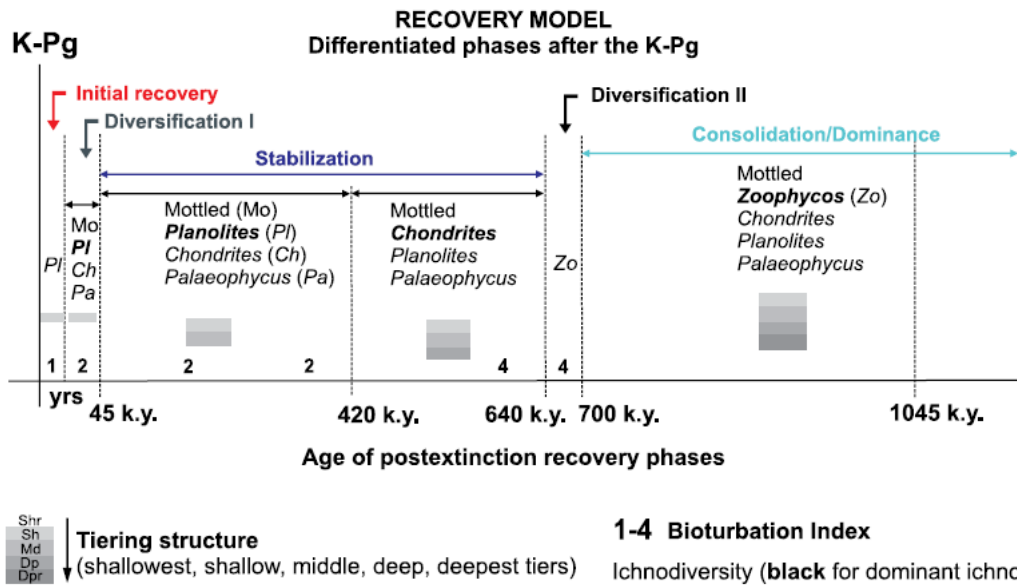
14

Figure 3. Proposed recovery model of macrobenthic tracemaker community after the Cretaceous-Paleogene (K-Pg) boundary impact with differentiated phases.

3. 三铁同位素限定了海洋铁汇在早期大气氧化作用中的角色

翻译人：冯婉仪 fengwy@sustech.edu.cn

*Heard A W, Dauphas N, Guilbaud R, et al. **Triple iron isotope constraints on the role of ocean iron sinks in early atmospheric oxygenation** [J]. Science, 2020, 370: 446-449 .*

https://doi.org/10.1126/science.aaz8821

摘要：铁在地球表面氧化作用中所起的作用是模棱两可的。铁可能通过形成海洋中三价铁氧氢氧化物消耗分子氧，或者它可能通过黄铁矿埋藏促进了大气氧化。通过对太古宙-古元古代沉积物和实验室合成黄铁矿的高精度铁同位素测量，我们发现新太古宙-古元古代黄铁矿的三铁同位素组成需要广泛的海洋铁氧化作用以及有限的硫黄铁矿化作用。利用这些资料提供的同位素分馏模型，我们限定了新太古代海相铁中的沉积三价铁氢氧化物和黄铁矿汇的相对大小。研究表明，黄铁矿的埋藏可能导致分子氧的输出超过局部二价铁氧化物的沉淀，从而促进太古宙地表环境早期的瞬时氧化作用。

ABSTRACT: The role that iron played in the oxygenation of Earth's surface is equivocal. Iron could have consumed molecular oxygen when Fe^{3+}-oxyhydroxides formed in the oceans, or it could have promoted atmospheric oxidation by means of pyrite burial. Through high-precision iron isotopic measurements of Archean-Paleoproterozoic sediments and laboratory grown pyrites, we show that the triple iron isotopic composition of Neoarchean-Paleoproterozoic pyrites requires both extensive marine iron oxidation and sulfide-limited pyritization. Using an isotopic fractionation model informed by these data, we constrain the relative sizes of sedimentary Fe^{3+}-oxyhydroxide and pyrite sinks for Neoarchean marine iron. We show that pyrite burial could have resulted in molecular oxygen export exceeding local Fe^{2+} oxidation sinks, thereby contributing to early episodes of transient oxygenation of Archean surface environments.
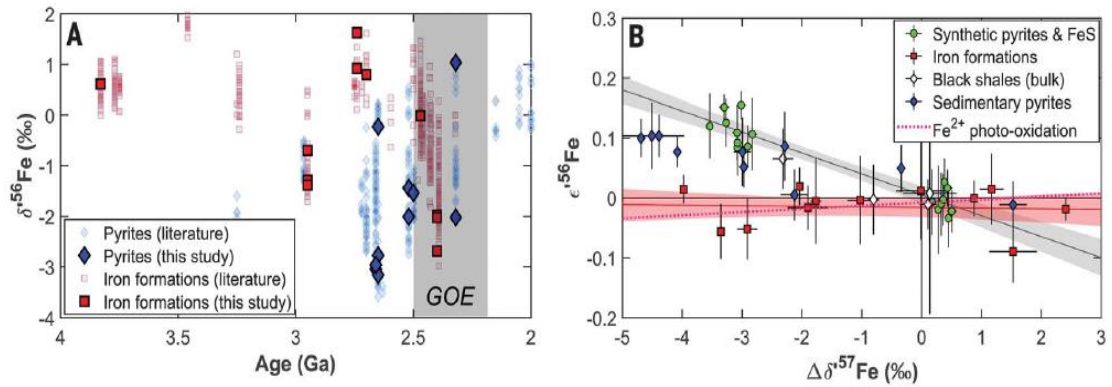
Figure 1. Iron isotope systematics of pre-GOE sediments and synthetic pyrites and FeS produced in laboratory experiments. (A) $\delta'^{56}Fe$ (relative to IRMM-014) values of IFs and pyrites analyzed in this study, plotted against their age [published IF and pyrite data compiled in (11) are also plotted for reference]. (B) Triple Fe isotopic systematics for IFs, pyrites, and black shales in $\varepsilon'^{56}Fe$ versus $\Delta\delta'^{57}Fe$ space. $\Delta\delta'^{57}Fe$ values are reported as differences from IRMM-014 and the starting material for the natural samples and the synthetic pyrites, respectively. Error bars and shaded areas are 95% confidence intervals. The slopes of endmember MFLs associated with iron-redox processes (red line and red shaded area) and KIEs during pyritization (black line and gray shaded area) are constrained through analysis of isotopically light, Mn-rich IFs and laboratory pyrites precipitated through the H2S pathway (14, 27, 40), espectively. The slope of the IF MFL agrees well with the theoretical hightemperature equilibrium limit law [defined by the horizontal axis, (20)] and an experimentally determined MFL for Fe^{2+} oxidation [determined by means of UV photo-oxidation (22)], which implies control by Fe^{2+}-Fe^{3+} equilibrium. Synthetic pyrite and FeS define a kinetic MFL for sulfide precipitation. Pre-GOE pyrites fall in an intermediate space between iron oxidation and pyritization endmembers.
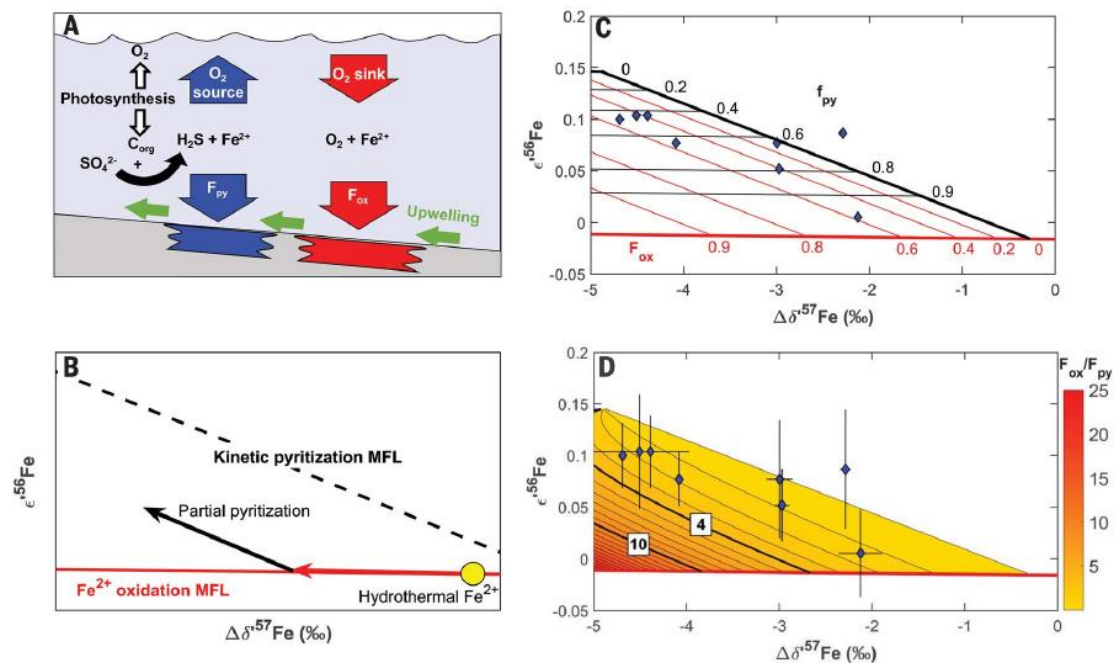

Figure 2. Interpretation of triple Fe isotope compositions of isotopically light pyrites. (A) Schematic

representation of the Fe sinks (F_{ox} and F_{py}), and their inferred links to O_2 cycling in the pre-GOE oceans. (B) Triple Fe isotopic interpretation of the two-step process involved in pyrite formation. Iron with starting composition resembling hydrothermal fluids (yellow circle; $\Delta\delta'^{57}Fe = -0.3‰$ relative to IRMM-014 with $\varepsilon'^{56}Fe$ on the empirical MFL defined by IFs) is oxidized, which drives residual Fe^{2+} to lighter $\delta'^{57}Fe$ compositions along the Fe^{2+} oxidation MFL. Partial pyrite precipitation from this residual Fe^{2+} subsequently causes fractionation along the kinetic pyritization MFL. The approach is detailed in fig. S5 with mathematical derivations provided in the supplementary materials (27). (C) Pyrite data and contours for F_{ox} and f_{py} in triple Fe isotopic space. Both Fe^{2+} oxidation and pyritization are modeled with Rayleigh distillations. Iron isotopic fractionation during iron oxidation is assumed to reflect the composition of residual dissolved Fe^{2+} experiencing fractional removal of Fe^{3+}-oxyhydroxide upon upwelling into oxidizing near surface waters. Iron isotopic fractionation during pyritization is assumed to reflect the composition of the cumulative product, as we analyzed relatively large pyrite nodules (27). The fraction of total upwelled Fe deposited as pyrite is calculated as $F_{py} = f_{py} \times (1 - F_{ox})$. (D) Pyrite data and contours of F_{ox}/F_{py} (relative size of oxyhydroxide and pyrite sedimentary Fe sinks). Bold contours at 4 and 10 indicate thresholds for net O_2 source versus sink behavior for volcanic H_2S/SO_2 inputs ratios of 1 (7) and 0 (8), respectively. In (B) to (D), $\Delta\delta'^{57}Fe$ values are reported as differences from IRMM-014.

4. 东赤道太平洋的大洋钻探 U1335 沉积物得到的过去 8 Myr 地磁场相对强度和倾角异常

翻译人：李园洁 liyj3@sustech.edu.cn

摘要：为了解地球发电机的机制比如古强度和极性间隔之间的关系和时间平均场的结构，连续的相对古强度和倾角异常记录非常必要，但是目前~3 Ma 之前的记录在时间和空间上都非常有限。本文作者对大洋钻探 U1335 在东赤道太平洋取得沉积物进行古地磁研究，获得过去~8 Ma 连续的相对古强度和倾角异常的记录。由于低的沉积速率 (~8.4 m/Myr 或更低)，记录的分辨率较低，但足够确定出长期变化。岩石磁学结果表明生物成因的磁铁矿是主要载磁矿物，而且~4 Ma 之前生物成因磁铁矿相对于陆源磁铁矿比例增加。~4-8 Ma 平均古强度比 0~4 Ma 的低将近 30%。在~4 Ma 古强度降低 50%，但可能其中的 20%是假的，是由生物成因磁铁矿比例增加导致的。过去~8 Myr 的古强度变化和极性间隔之间没有相关性。在过去~5 Myr 倾角异常的幅值在反极性期间(4.43° ± 1.47°)比正极性期间(-0.69° ± 2.98°)稍微高，与这期间可用的 TAF 模型一致。~6 Ma 之前,倾角异常的符号在正极性期间可能转变为正，在反极性时可能比~5 Ma 之后的稍微高点。

ABSTRACT：For understanding the fundamentals of the geodynamo such as the relation between paleointensity and polarity length and time-averaged field (TAF) structure, continuous records of relative paleointensity (RPI) and inclination anomaly (ΔI) are desired; however, available records older than ~3 Ma are still very limited in time and space. We conducted a paleomagnetic study of the Integrated Ocean Drilling Program Site U1335 sediments in the eastern equatorial Pacifific to obtain continuous RPI and ΔI records since ~8 Ma. Slow deposition, ~8.4 m/Myr or less, limits the resolution of the records but did allow for determination of long-term variations. Rock-magnetic measurements showed that biogenic magnetite dominates the magnetic mineral assemblages, and

the proportion of biogenic to terrigenous magnetic minerals increases prior to ~4 Ma. The average paleointensity between ~4 and 8 Ma is approximately 30% lower than that from 0 to ~4 Ma. The apparent reduction of RPI at ~4 Ma reaches approximately ~50%, but ~20% of this is estimated to be artificial, induced by the increase in the proportion of biogenic magnetite. No relation between paleointensity and polarity length is recognized for the last ~8 Myr. The magnitude of ΔI is slightly larger during reversed polarity chrons (4.43° ± 1.47°) than normal polarity chrons (-0.69° ± 2.98°) over the last ~5 Myr, which agrees with the available TAF models of this time span. Prior to ~6 Ma, the sign of ΔI during the normal chrons might have switched to positive, and ΔI during reversed chrons might have been slightly larger than that after ~5 Ma.

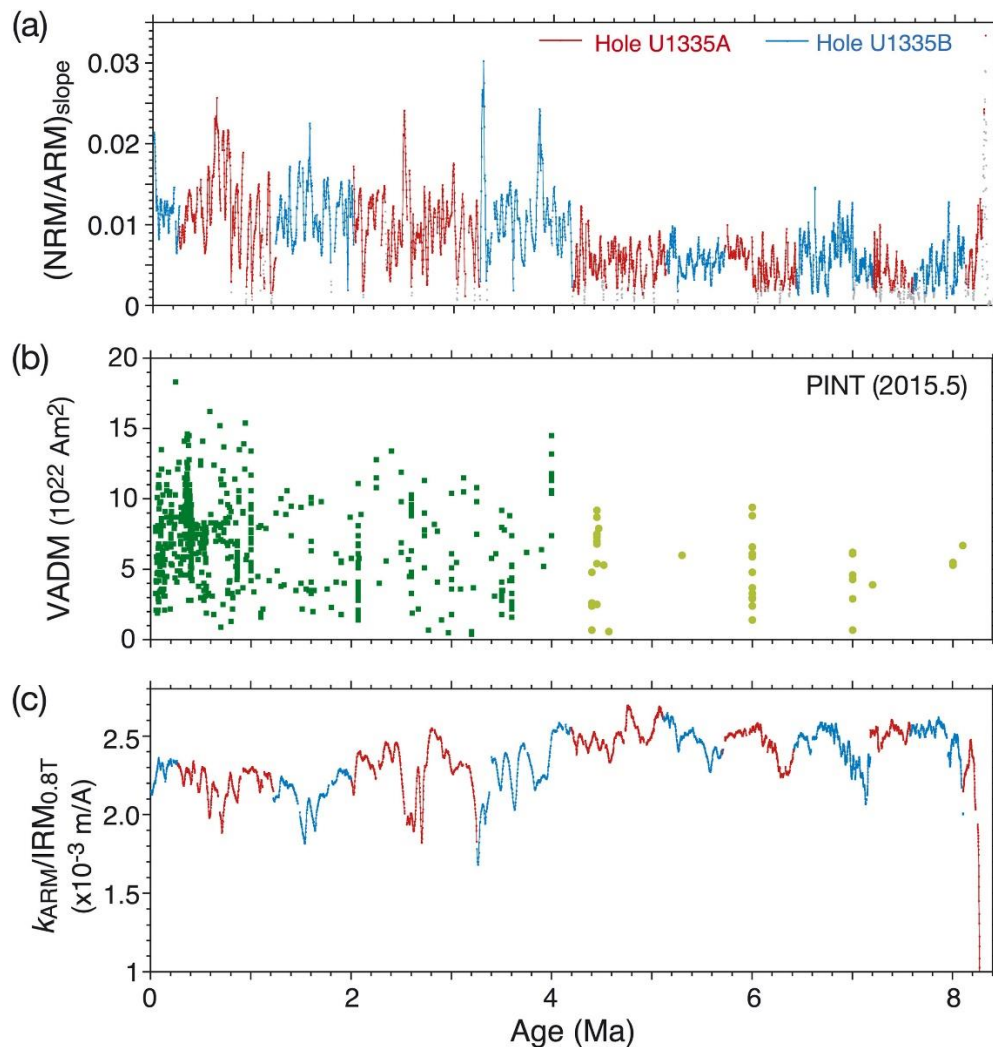Figure 1. (a) Temporal variations in relative paleointensity obtained from the slopes of the natural remanent magnetization (NRM) versus anhysteretic remanent magnetization (ARM) demagnetization plots, (b) absolute paleointensity data of volcanic rocks extracted from the PINT database (Biggin et al., 2009) by applying the selection criteria that the data were an average of three or more individual

specimens and their dispersion was less than 15% of the average, and (c) the kARM/ isothermal remanent magnetization ratio. The red and blue colors in panels (a) and (c) represent data from Holes U1335A and U1335B, respectively, along the composite section. VADM = virtual axial dipole moment.
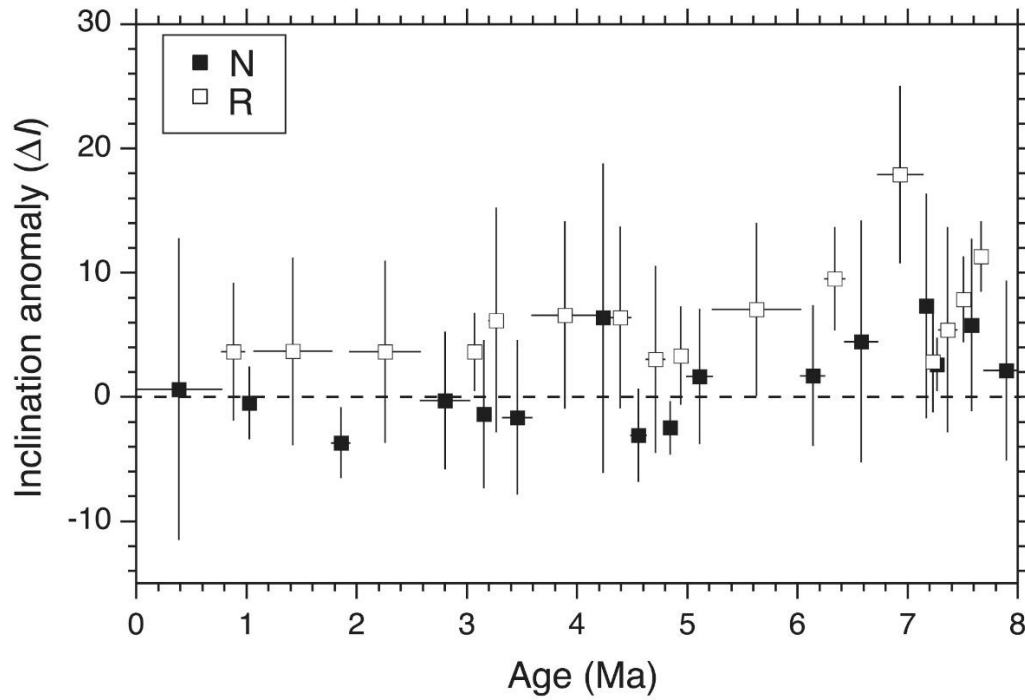

Figure 2. Inclination anomaly (ΔI) averaged over each polarity chron. The vertical error bar shows the uncertainty (see text) and the horizontal bar represents a time span of each polarity chron. The solid and open symbols represent normal and reversed polarity periods, respectively.

5. 二叠纪至三叠纪生物大灭绝突然加剧 — 海洋碳循环扰动的驱动作用

翻译人：柳加波

摘要：大约 251.9 百万年前的二叠纪/三叠纪界线标志着地质记录中发现的决定了生命演化方向的严重环境危机。来自西伯利亚地盾的岩浆作用被认为起了重要作用，但是因果关系的触发及其反馈机制尚未充分理解。本文，我们从沉积在特提斯陆架上的化石腕足动物壳中重建了新的基于硼同位素的海水 pH 记录。该记录表明随着晚二叠纪大规模灭绝的开始，海水 pH 值急剧下降。结合碳同位素数据，我们的结果被整合到一个地球化学模型中，该模型解决了碳循环动力学以及海洋氧化还原条件和氮同位素转换的问题。我们发现，最初的海洋酸化与西伯利亚基岩侵入导致的突然大量碳释放密切相关。我们揭示了温室效应对海洋环境的影响，并表明在三叠纪最早期，由于化学风化速率增加而引起的海表温度升高，输出生产力和养分输入，并导致广泛的脱氧和零星的硫化物中毒。我们的发现使我们能够对导致最大的显生宙大灭绝事件的生物地球化学机制进行一致的整合。

ABSTRACT: The Permian/Triassic boundary approximately 251.9 million years ago marked the most severe environmental crisis identified in the geological record, which dictated the onwards course for the evolution of life. Magmatism from Siberian Traps is thought to have played an important role, but the causational trigger and its feedbacks are yet to be fully understood. Here we present a new boron-isotope-derived seawater pH record from fossil brachiopod shells deposited on the Tethys shelf that demonstrates a substantial decline in seawater pH coeval with the onset of the mass extinction in the latest Permian. Combined with carbon isotope data, our results are integrated in a geochemical model that resolves the carbon cycle dynamics as well as the ocean redox conditions and nitrogen isotope turnover. We find that the initial ocean acidification was intimately

linked to a large pulse of carbon degassing from the Siberian sill intrusions. We unravel the consequences of the greenhouse effect on the marine environment, and show how elevated sea surface temperatures, export production and nutrient input driven by increased rates of chemical weathering gave rise to widespread deoxygenation and sporadic sulfide poisoning of the oceans in the earliest Triassic. Our findings enable us to assemble a consistent biogeochemical reconstruction of the mechanisms that resulted in the largest Phanerozoic mass extinction.
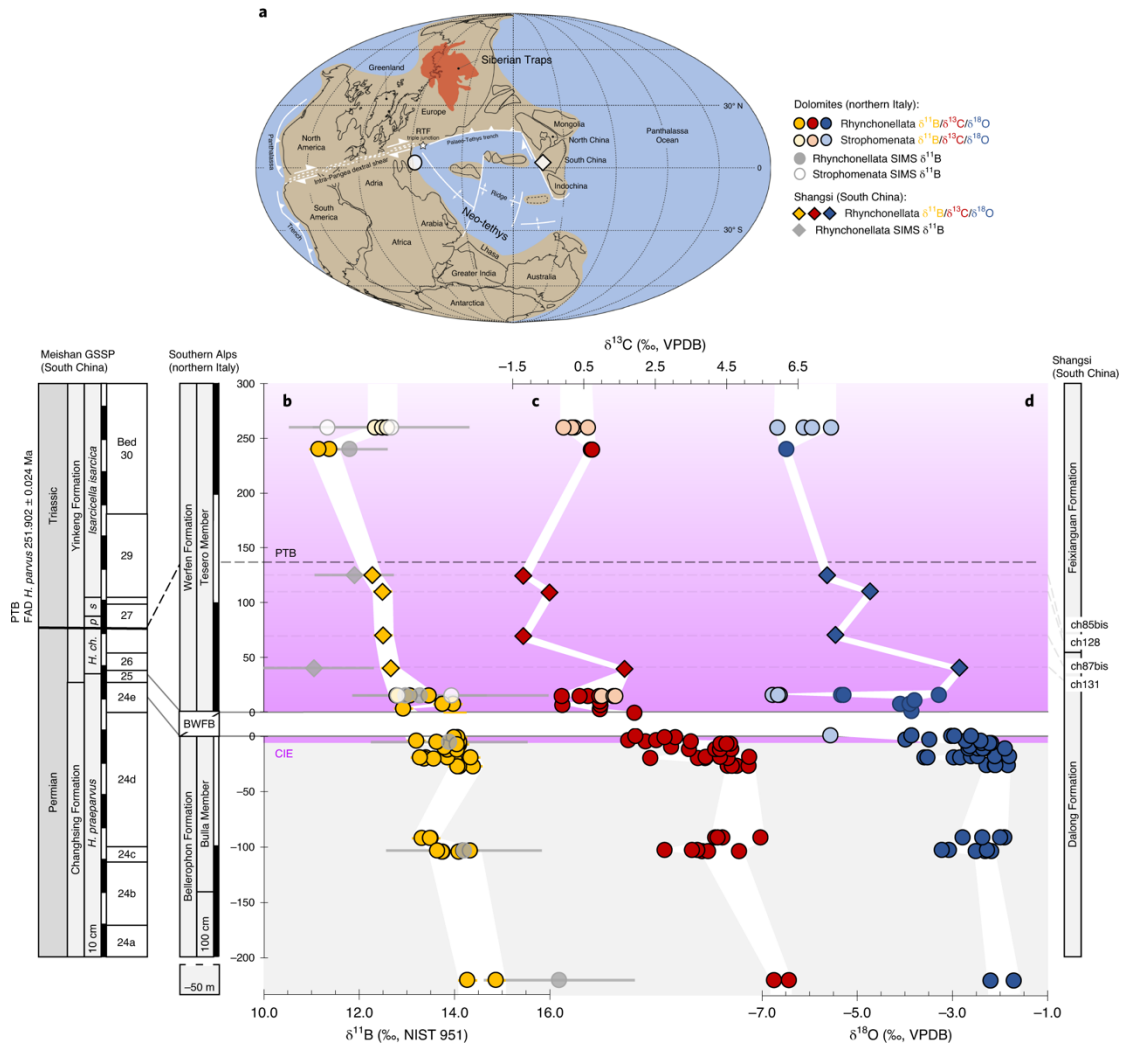
Figure 1. **a**, Late Permian palaeogeographic reconstruction(Methods) with the locations of the sampling sites. **b–d**, $\delta^{11}B$ (**b**), $\delta^{13}C$ (**c**) and $\delta^{18}O$ (**d**) records derived from brachiopod shells from Southern Alps (Sass de Putia, Tesero and Val Brutta) and South China (Shangsi). The error bars in **b** indicate the analytical uncertainty for solution-based $\delta^{11}B$ (2 s.d. = 0.2‰) and the s.d. between multiple ion spots measurements within a single shell for SIMS $\delta^{11}B$. The stratigraphy of the Meishan Global Boundary Stratotype Section and Point (GSSP) is shown for comparison. The purple field marks the onset of the CIE as defined in our age model(Methods and Supplementary Information), with the geochronology based on the latest age estimates. Conodont zones: *Hindeodus*

23

praeparvus, *H. changxingensis*, *H. parvus*, *Isarcicella staeschei* and *I. isarcica*. BWFB, Bellerophon–Werfen Formation boundary; FAD, first appearance datum; Ma, million years ago; NIST, National Institute of Standards and Technology; VPDB, Vienna Pee Dee Belemnite; RTF, ridge trench fault.

6. 南海中央裂谷系统三维演化

翻译人：刘伟 inewway@163.com

摘要：裂谷边缘是大陆岩石圈伸展、裂解和向海底扩张过渡的结果，其模式通常由端元概念模型所描述。然而，目前的地球物理数据对这些模型提出了挑战，显示出更复杂的裂谷作用类型谱。本文结合地球物理和地质观测资料，对南海中部裂谷系的时空演化进行了约束。通过平行于南海中央裂谷系伸展方向的地震剖面，我们对南海中央裂谷系的大陆伸展机制和大海陆过渡带(COT)的形成有了新的认识。我们展现了一个约 850 km 宽的大陆地壳区域，在这里分布的伸展变形表现为由 7 个 100～200 km 长的构造段（岩石圈石香肠构造）组成。每一段主要是由 18-24 km 厚的地壳组成，其侧向变薄的石香肠颈仅为 10 km（ß 因子 6.5～3.3）。钻探和地层资显示，在南海中部的 6 个石香肠颈持续伸展，直到 23 Ma 左右，海底扩张传播到了其中一个石香肠颈。我们认为，从早期裂谷到破裂，这 7 个裂谷段演化为相互独立的子系统。南海东北、西南共轭边缘均发育构造等效的超薄壳地堑，支持了南海三维宽裂谷变形模式。六个超薄地壳同生颈和 COT 的突变性质和位置支持了该断裂不是由大陆岩石圈进一步减薄控制的，而是由海底向西南方向的扩张传播决定的。

ABSTRACT: Rifted margins result from continental lithosphere extension, breakup, and transition to seafloor spreading by modes typically described by end-member conceptual models. However, current geophysical data challenge these archetypes showing a more complex spectrum of rifting styles. Here, we integrate geophysical and geological observations to constrain the time and space evolution of the central South China Sea (SCS) rift system. We provide new insights into the continental extension mechanisms and continent-ocean transition (COT) formation from a seismic transect parallel to the extensional direction of the central SCS rift system. We present a ~850 km wide region of continental crust where distributed extensional deformation formed a pattern of lithospheric boudinage defined by seven 100-200 km long structural segments. Each segment is

formed by an 18-24 km thick crust sector laterally thinning into an interboudin neck with ≤10 km ultra-thin crust (ß factors ~3.3-6.5). Drill and stratigraphic information support that extension continued at all six interboudin necks in the central SCS until ~23 Ma, when breakup by seafloor spreading propagation reached one of them. We propose that the seven segments evolved as discrete subsystems from early rifting to breakup. Structurally equivalent ultra-thin-crust grabens occur NE and SW of both SCS conjugate margins, supporting a 3D wide-rift mode of deformation across the SCS rift system. The six ultra-thin crust contemporaneous necks and the abrupt nature and location of the COT support that the breakup was not controlled by further continental lithospheric thinning but rather was determined by the seafloor spreading propagation towards the SW.
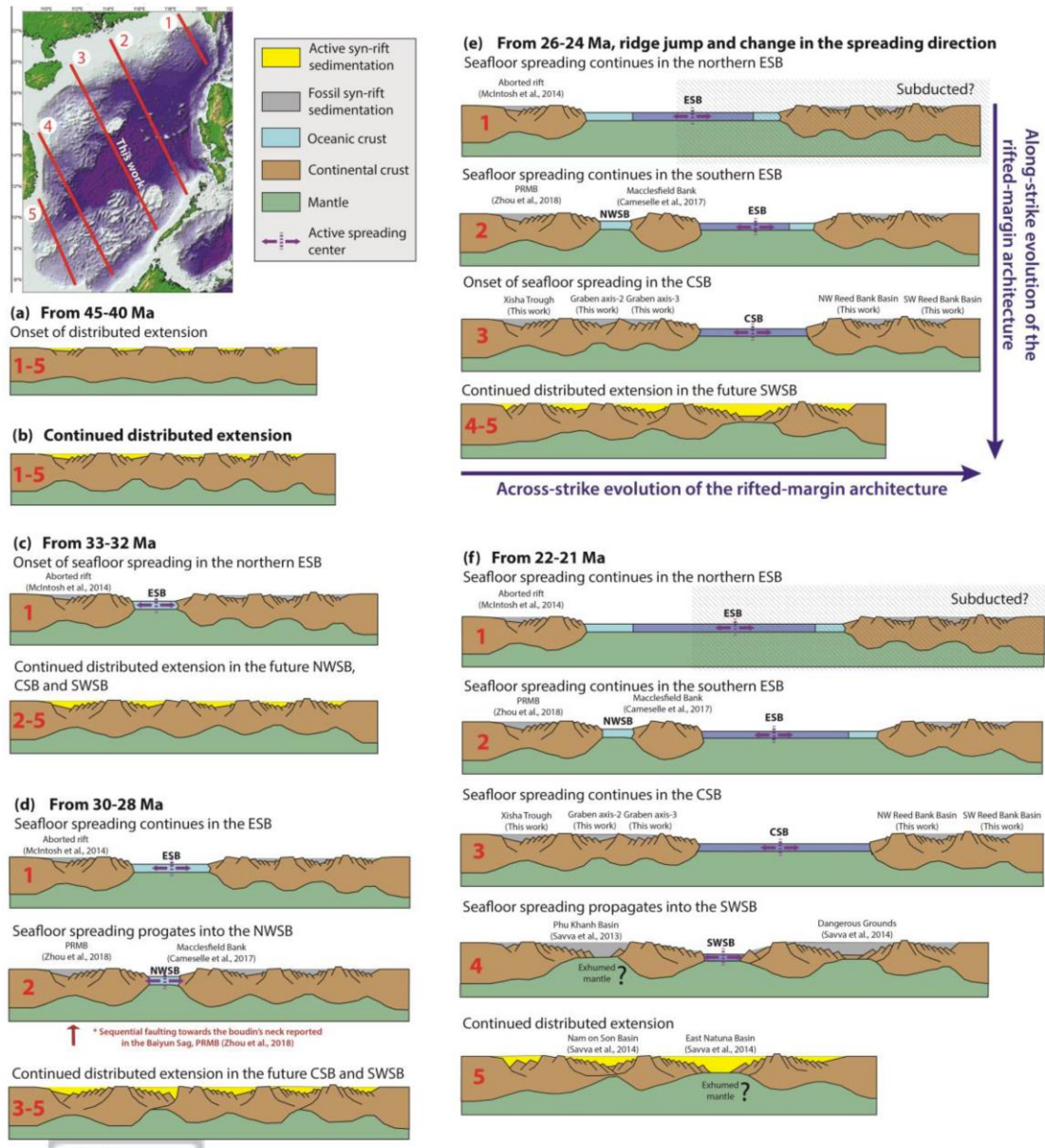
Figure 1. Cartoons illustrating the temporal and spatial evolution of the SCS rift system (not to scale). Red numbered lines in the map corresponds to schematic cross-sections depicted in rift stages shown in a) to e). Cross-section 3 is the seismic transect presented in this work.

7. 前罗马山顶定居点（**Monte Torretta diPietragalla**）的地球物理初步调查结果

翻译人：曹伟 11930854@QQ.com

摘要：蒙特托雷塔(Pietragalla, PZ)代表了古卢卡尼亚最有趣并鲜为人知的定居点之一。在过去的 50 年里，多次考古活动对该遗址进行了调查，但到目前为止还没有结果发表。为了研究和宣传该遗址的考古价值，巴黎大学与柏林洪堡大学共同建立了 Pietragalla 联合项目。该项目基于多学科的方法，旨在研究定居点，并恢复以前考古工作中丢失的信息。在遗址上进行的第一次地球物理勘探提供了重要的成果，增加了对遗址的了解，并将有助于考古学家今后的调查。通过综合对比不同的地球物理方法，包括探地雷达、电阻率层析成像和地磁测量，在防御墙的附近和遗址的两个大门处获得了多种信息。此外，地质和地貌解释突出了考古遗址的重要信息。研究结果反映了地球物理活动在上世纪农村活动严重破坏的背景下具有重要意义。从考古角度来看，2017 年和 2018 年进行的地球物理调查显示，围墙所围区域内建筑活动密集。正是通过这些研究结果，我们如今才能够了解 longue durée 地区（至少在 infra-muros 地区西部）的定居点模式。

ABSTRACT: Monte Torretta (Pietragalla, PZ) represents one of the most interesting and less known settlements of ancient Lucania. The site was investigated in the last 50 years by several archaeological activities, but no result has been published so far. In order to study and disseminate the archaeological value of the site, the Université Paris1 Panthéon-Sorbonne and the Humboldt-Universität zu Berlin has established the joint Pietragalla Project. The project is based on a multidisciplinary approach, which aims at studying the settlement and at recovering the lost information obtained by the previous archaeological works. The first geophysical activities conducted on the site offer important results, which increase the knowledge of the site and will help the archaeologists in their future investigation. Through the comparison and integration of different

geophysical methodologies, including ground penetrating radar, electrical resistivity tomography and geomagnetic measurements, various information was obtained in proximity of the fortification walls and the two main gates of the site. Moreover, geological and geomorphological interpretations highlighted important information on the archaeological site. The obtained results show the importance of geophysical activities in a context strongly damaged by rural activities of the last century. From an archaeological point of view, the geophysical surveys con-ducted in 2017 and 2018 show a dense building activity within the area enclosed by the walls. Thanks to these results, we are now able to understand the settlement pattern in the longue durée, at the least for the western part of the infra-muros area.
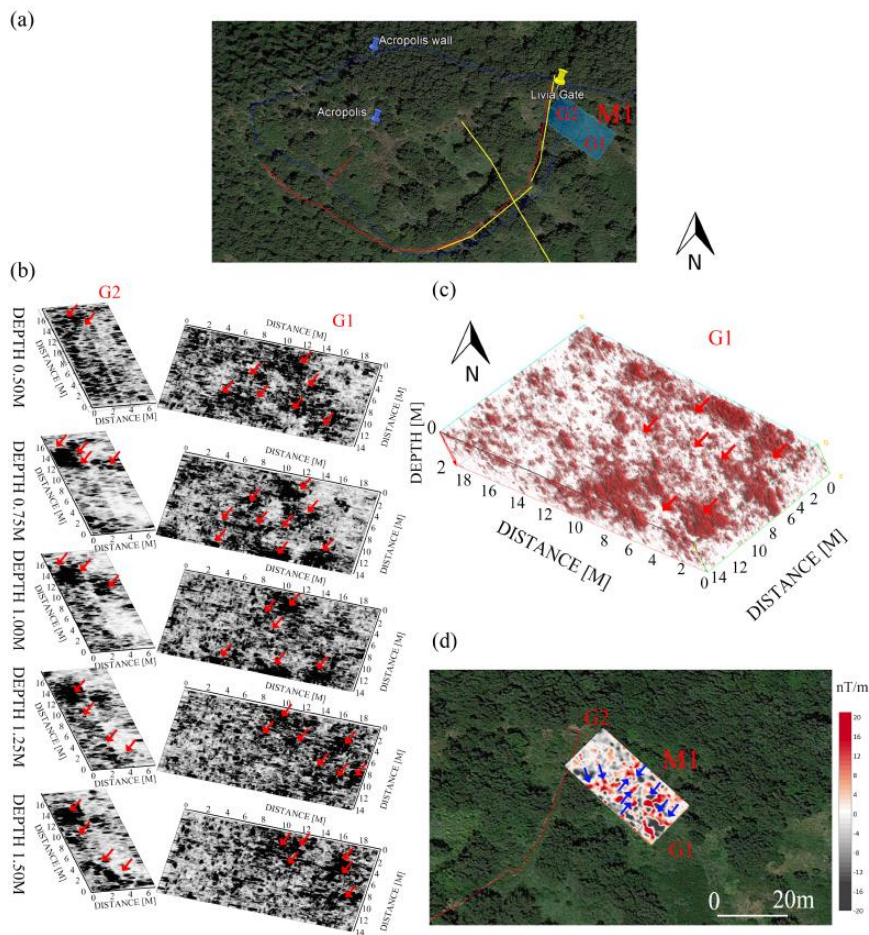

Figure 1. The 3D GPR and MAG acquisition carried out near the Livia Gate (a), with GPR depth slices excreted every 0.25 m (b) from the 3Dmodel (c) and comparison with the Acropolis geomagnetic map acquired in front of the gate (d).

8. 中国西南地区在早全新世夏季温度和季风降雨的解耦

翻译人：杨会会 11849590@mail.sustech.edu.cn

摘要：全新世温度指标重建表明，在不同地区温度最大值的时间和幅度都有很大差异。考虑到"全新世温度难题"对于重建季节性温度变化变得越来越重要。作为全球季风系统的主要组成部分，印度夏季季风(ISM)从热带海洋向高纬度地区输送湿热，因此对其影响区域具有重大的社会经济意义。我们从中国西南星云湖中建立了 14,000 年以来的，基于孢粉重建起来的夏季温度记录(MJT)；中国西南部的星云湖气候受 ISM 支配。MJT 在新仙女木时期下降，在 8000-5500 yr BP 期间缓慢上升至高值，之后下降。MJT 记录与同一沉积物岩芯碳酸盐氧同位素($\delta^{18}O$)推断的记录不同。后者反映了季风降水的变化，最高降水出现在全新世早期(11000-6500 yr BP)。我们认为在全新世早期，中国西南地区的夏季温度和降水是解耦的。MJT 和季风降水在全新世中期后均有所减少，与北方夏季日照趋势一致。我们认为，与高降水和强夏季季风相关的云量增加可能降低了全新世早期的温度，否则，温度应受控于夏季日照的增加。高纬度地区融化的冰盖和全新世早期大气中高浓度的气溶胶也可能部分地导致了该区夏季相对较冷的温度。

ABSTRACT: Proxy-based reconstructions of Holocene temperature show that both the timing and magnitude of the thermal maximum varied substantially across different regions. Given the 'Holocene temperature conundrum', it is becoming increasingly important to reconstruct seasonal temperature variations. As a major component of the global monsoon system, the Indian summer monsoon (ISM) transports moisture and heat from the tropical oceans to higher latitudes and thus it has substantial socioeconomic implications for its regions of influences. We developed a well-dated, pollen-based summer temperature record (mean July; MJT) for the last 14,000 years from Xingyun Lake in southwest China, where the climate is dominated by the ISM. MJT decreased during the Younger Dryas, increased slowly to high values during 8000-5500 yr BP, and decreased thereafter.

The MJT record differs from that inferred using carbonate oxygen isotopes ($\delta^{18}O$) from the same sediment core. The latter record reflects variations in monsoon precipitation, with highest precipitation during the early Holocene (11,000-6500 yr BP). We propose that summer temperature and precipitation in southwest China were decoupled during the early Holocene. Both MJT and monsoon precipitation decreased after the middle Holocene, tracking the trend in boreal summer insolation. We suggest that greater cloud cover, associated with high precipitation and generated by a strong summer monsoon, may have depressed early Holocene temperatures that would otherwise be driven by greater summer insolation. Melting ice sheets in high-latitude regions and high concentrations of atmospheric aerosols during the early Holocene may also have contributed, in part, to the relatively cool summer temperatures.
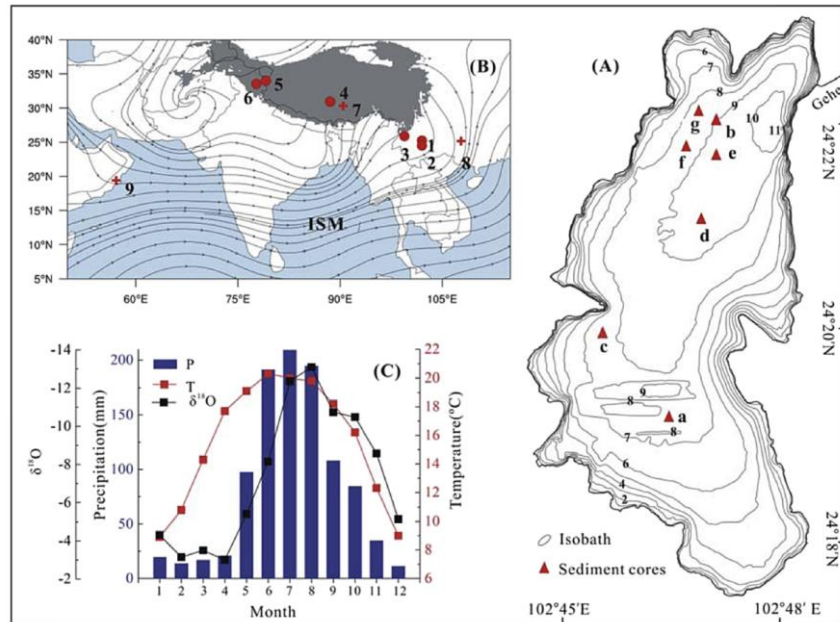

Figure 1. Hydrological and climate information for the study area. (A) Bathymetry of Xingyun Lake and sediment core locations: a - XH-14-X-94 (Hodell et al., 1999); b - XYA09 (Hillman et al., 2014); c - core published in Zhang et al. (2014); d - XY08A (Chen et al., 2014a); e - XY08C, (Yu JQ, unpublished); f - XYB08 (Hillman et al., 2017); g - XH-3-IV-89 (Whitmore et al., 1994). (B) Main study sites in the Indian Summer Monsoon (ISM)-dominated region: 1 - Xingyun Lake (this study); 2 - Qilu Lake; 3 - Tiancai Lake; 4 - Selin Co; 5 - Bangong Co; 6 - Tso Moriri Lake; 7 - Tianmen Cave; 8 - Dongge Cave; 9 - Qunf Cave, Oman. Background is the June-July-August (JJA) mean 850-hPa isohyet during the period 1971-2000; areas above 3000 m a.m.s.l. are shaded in grey. (C) Monthly average temperature, precipitation and oxygen isotope values from 1986 to 2003 at the Kunming GNIP station (IAEA/WMO).
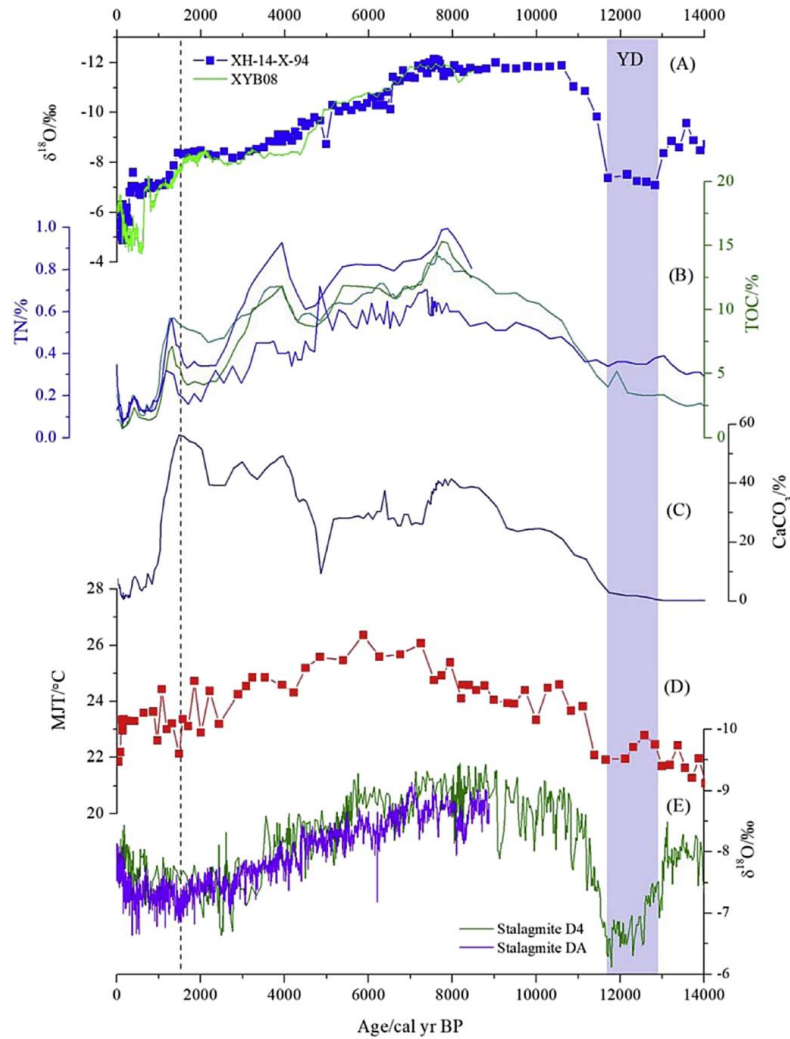
Figure 2. Multiple variables in the Xingyun Lake sediment and their comparison with the speleothem δ¹⁸O record from Dongge Cave. (A) Lacustrine carbonate d¹⁸O records from Xingyun Lake; green line is the record from core XYB08 (Hillman et al., 2017) and the blue line with squares is from core XH-14-X-94 (Hodell et al., 1999); (B) TOC (green) and TN (blue) records from cores XH-14-X-94 (long record) and XY08A (short record); (C) carbonate content of core XH-14-X-94 (Hodell et al., 1999); (D) pollen-based mean July temperature (MJT) reconstruction from Xingyun Lake; (F) speleothem (D4 and DA) oxygen isotope records from Dongge Cave (Dykoski et al., 2005; Wang et al., 2005). The vertical bar indicates the YD event and the dashed line represents the onset of increasing human activity in the catchment (Wu et al., 2015a). (For interpretation of the references to color in this figure legend, the reader is referred to the Web version of this article.)

9. 黑海沉积物的 Laschamps 地磁极性偏移记录：磁铁矿与胶黄铁矿，离散样本与 U-channels 数据

翻译人：王浩森 11930841@mail.sustech.edu.cn

摘要：根据离散样本和其中一个岩芯中的 U-channels 数据，对黑海东南部两个不同水深的沉积物岩芯进行了磁性地层学研究，得到了过去约 68 ka 的高分辨率地磁场强度记录。年龄限制是由三个已知年龄的 tephra 层，加速器质谱法 ^{14}C 测年以及通过 X 射线荧光扫描获得的元素比值与格陵兰冰芯的氧同位素记录来提供的。沉积速率从全新世的最低约 5 cm ka-1 到冰期海洋同位素第 4 阶段的最高 50 cm ka-1 不等。完全反转的倾角和偏角数据，以及~41 ka 的相对古强度的明显降低提供了 Laschamps 地磁极性偏移的证据。在其中一个岩芯中，Mono Lake 在 34.5 ka 处的记录也可能发生了逆转。然而，古地磁记录在一定程度上受到胶黄铁矿的影响。通过饱和磁化强度与体积磁化率之比的排除标准，从古地磁数据中删除了含胶黄铁矿的样品。因此，在古地磁记录中仅剩下 25-55％的样品是从较浅的取芯位置的沉积物获得的。但是在更深位置的离散样本和 U-channels 的古地磁记录受胶黄铁矿的影响要小得多。对比古地磁数据表明，两种采样技术均可以一定程度上恢复 Laschamps 极性偏移的主要特征。但是，由于存在带有异常方向的胶黄铁矿，必须从 U-channels 记录中删除几个层位。通过与离散样本数据进行比较，还可以观察到 U-channels 记录中的一些定向假像，这些假像是由广泛的磁力计响应函数的低通滤波引起的，这些假像一般是在快速定向和大幅度变化中求平均值。因此，当研究地磁场快速变化（例如反转和偏移）时，采用离散采样的高分辨率采样应该是首选的。

ABSTRACT: Magnetostratigraphic investigation of sediment cores from two different water

depths in the SE Black Sea based on discrete samples, and parallel U-channels in one of the cores, yielded highresolution records of geomagnetic field variations from the past about 68 ka. Age constrains are provided by three tephra layers of known age, accelerator mass spectrometry 14C dating, and by tuning element ratios obtained from X-ray fluorescence scanning to the oxygen isotope record from Greenland ice cores. Sedimentation rates vary from a minimum of ~5 cm ka−1 in the Holocene to a maximum of ~50 cm ka−1 in glacial marine isotope stage 4. Completelyreversed inclinations and declinations as well as pronounced lows in relative palaeointensity around 41 ka provide evidence for the Laschamps geomagnetic polarity excursion. In one of the investigated cores also a fragmentary record of the Mono Lake excursion at 34.5 ka could be revealed. However, the palaeomagnetic records are more or less affected by greigite, a diagenetically formed magnetic iron sulphide. By definition of an exclusion criterion based on the ratio of saturation magnetization over volume susceptibility, greigite-bearing samples were removed from the palaeomagnetic data. Thus, only 25–55 per cent of the samples were left in the palaeomagnetic records obtained from sediments from the shallower coring site. The palaeomagnetic record from the deeper site, based on both discrete samples and U-channels, is much less affected by greigite. The comparison of palaeomagnetic data shows that the major features of the Laschamps polarity excursion were similarly recovered by both sampling techniques. However, several intervals had to be removed from the U-channel record due to the presence of greigite, carrying anomalous directions. By comparison to discrete sample data, also some directional artefacts in the U channel record, caused by low-pass filtering of the broad magnetometer response functions, averaging across fast directional and large amplitude changes, can be observed. Therefore, high-resolution sampling with discrete samples should be the preferred technique when fast geomagnetic field variations, such as reversals and excursions, shall be studied from sedimentary records in the very detail.
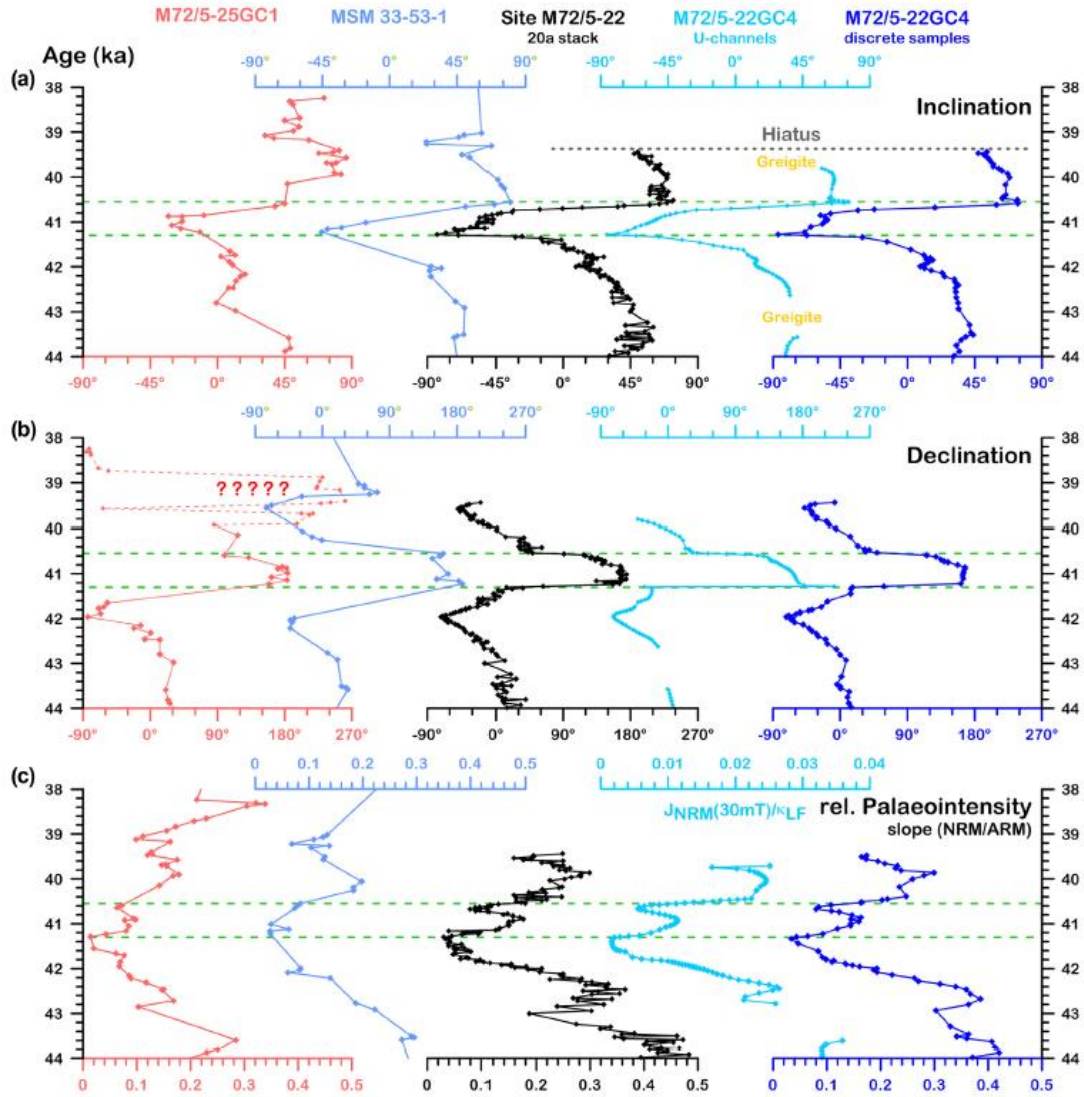
Figure 1. Compilation of time series of the Laschamps excursion for the time interval from 44 to 38 ka derived from SE BlackSea sediments. Inclination(a), declination (b), and relative palaeointensity (c) from individual cores M72/5–25GC1 and MSM33–53-1 (left-hand panel) and from core M72/5–22GC4, both from U-channels and discrete samples (right-hand panel), are shown together with the stacked data from site M72/5–22 (middle panel). Results from MSM33–53-1 are shown from samples with SIRM/kLF ≤ 12.5 kAm−1. Question marks indicate doubtful declinations, though not affected by greigite, in core M72/5–25GC1, not seen in the (fragmentary) record from MSM33–53-1 from about the same site. As indicated in (a), gaps in the U channel data from core M72/5–22GC4 are due to eliminated intervals with anomalous directions carried by greigite. The horizontal green dashed lines mark the totally reversed field during the Laschamps excursion in the Black sea area. Data from site M72/5–22 are cut off due to a hiatus starting at 39.4 ka, indicated by the horizontal black dotted line (only in a).

10. 太平洋和大西洋千年尺度气候变化的阶段性

翻译人：郑威　11930589@mail.sustech.edu.cn

摘要：来自阿拉斯加湾的新的放射性碳和沉积学结果表明重组的太平洋通风与Cordilleran冰盖快速消融同步，在千年尺度上反复发生，表明了过去4.2万年中冰-海动力学的密切耦合。北太平洋中层水通风随亚洲季风的强度变化而变化，支持了北太平洋古气候水汽和热从低纬度地区输送。中层水的碳十四年龄与cordilleran冰筏碎屑传输的峰值一致，都发生在劳伦冰盖消融事件之前，即Henrich事件。这个时间点排除了大西洋变化引发Cordilleran冰盖退缩的可能性，相反，说明了太平洋是一系列具有全球影响的动态气候事件的早期组成部分。

ABSTRACT: New radiocarbon and sedimentological results from the Gulf of Alaska document recurrent millennial-scale episodes of reorganized Pacific Ocean ventilation synchronous with rapid Cordilleran Ice Sheet discharge, indicating close coupling of ice-ocean dynamics spanning the past 42,000 years. Ventilation of the intermediate-depth North Pacific tracks strength of the Asian monsoon, supporting a role for moisture and heat transport from low latitudes in North Pacific paleoclimate. Changes in carbon-14 age of intermediate waters are in phase with peaks in Cordilleran ice-rafted debris delivery, and both consistently precede ice discharge events from the Laurentide Ice Sheet, known as Heinrich events. This timing precludes an Atlantic trigger for Cordilleran Ice Sheet retreat and instead implicates the Pacific as an early part of a cascade of dynamic climate events with global impact.
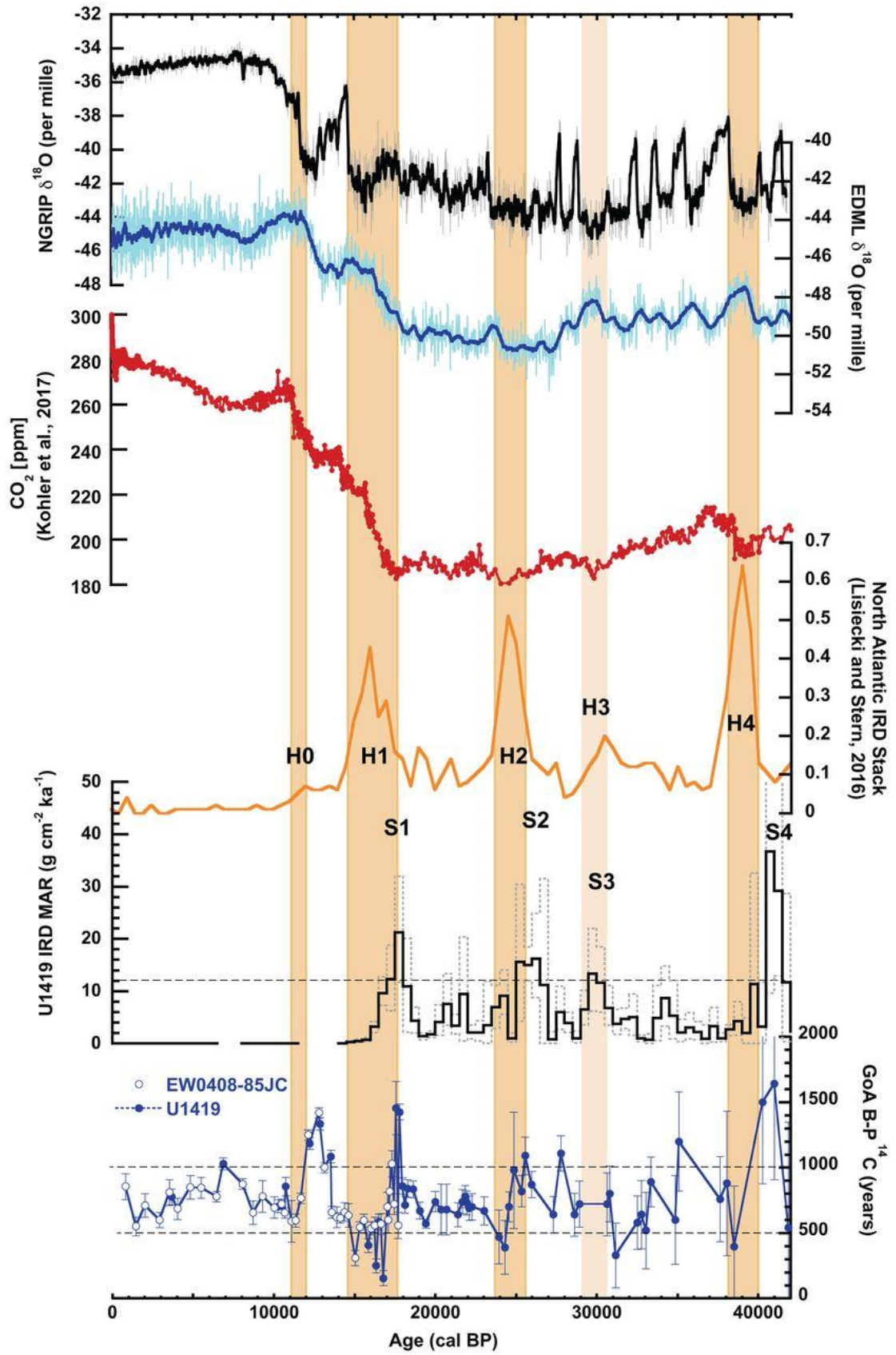
Figure 1. Global records of climate changes during the latest Pleistocene. Greenland [d18O from North Greenland Ice Core Project (NGRIP), black; 100-year smoothing shown in bold]

(61) and Antarctica (d18O from EDML, blue; 100-year smoothing shown in bold) (62) are shown on the synchronized AICC2012 time scale (63). Global atmospheric CO2 from ice cores plotted in red (64). Atlantic ice-rafted debris stack [normalized units in orange (65)] and U1419 IRD MAR calculated over 500-year increments (black) with ±1s uncertainty envelope (dashed gray lines). U1419 B-P 14C (blue, ±1s uncertainty; EW0408-85JC data denoted by open symbols). Timing of the North Atlantic Heinrich events shown in light orange bars; H1 to H4 from synthesis of (65), H0 from (66). The dashed line on the U1419 IRD panel denotes the level of 12 g cm−2 ka−1 that define Siku events 1 to 4. The dashed straight lines on the U1419 B-P panel denote 1000 and 500 years; Siku events are associated with regional B-P 14C age differences >1000 years, whereas Heinrich events are associated with values <500 years.

11. 第四纪晚期印度季风和西风在喜马拉雅山和东非冰川变化中的作用

翻译人：李海 12031330@mail.sustech.edu.cn

摘要：本文综述了喜马拉雅和东非地区第四纪晚期气候及冰川的变化，重点讨论印度夏季风 (ISM)，东非季风和西风的作用。主要对印度、喜马拉雅及东非地区 50 ka BP 以来的湖泊、泥炭、石笋、海洋沉积物及冰芯的高分辨记录进行多参数的分析研究。将利用 REMO-ESM 模型讨论参数的意义。研究结果表明，~17.0-15.0 ka BP 以来喜马拉雅山脉西部及东非地区均为大干旱期，全新世早期（10.0-7.0 Ka BP）受西风的影响降水逐渐增加。模型结果表明，西风对喜马拉雅山西北部影响较大，对喜马拉雅山西部的影响较小，冬季较低的日照促进了 LGM 期间冰川的发展。将不同地区的冰川变化与代用指标进行比较，以了解上述季风系统的响应，包括其驱动力。结果表明，西风是晚第四纪喜马拉雅西北部气候及冰川活动的主要驱动力。全新世早期和晚期冰川波动主要由喜马拉雅西北部的西风降水控制，而 ISM 则控制了第四纪晚期第四代喜马拉雅山的冰川波动。

Abstract This paper presents a review of Late Quaternary climatic changes and glacier variability in the Himalaya and East Africa, focusing on the role of Indian Summer Monsoon (ISM), East African monsoon, and Westerlies monsoons. Multi-proxy studies which are based on five different archives (lakes, peat bogs, speleothems, marine sediments, and ice cores) including sixty-five records from India and nearby regions, particularly in the Himalaya and in addition to seven archives from the equatorial Eastern part of Africa encompasses with high-resolution published and unpublished records for the last 50 ka BP. The proxy data is discussed towards REMO-ESM model Coupled Model Intercomprasion Project phase 5 (CMIP5 Project) results. Our results indicate that both Western Himalaya and East Africa had undergone mega-droughts from ~17.0-15.0 ka BP, and precipitation had increased during the Early Holocene (10.0-7.0 Ka BP) during the time span when the Westerlies dominated regions. The model results suggest that the Westerly monsoon has significantly contributed to the Northwestern Himalaya and somewhat to a lesser degree to the Western Himalaya and lower solar insolation in the winters did support the glacier advance during the LGM. The time series from the proxy data are compared with glacier fluctuations in different valleys to understand the response of the aforementioned monsoon system including other forcing factors which drive these variabilities. The review results indicate that the Westerlies was the main

driver of the climate and glacier fluctuations in Northwestern Himalaya during the Late Quaternary. The Early and Late Holocene glacier fluctuation was mainly controlled by Westerlies precipitation in Northwestern Himalaya and the ISM controlled the glacier fluctuations in the Western Himalaya during Late Quaternary.
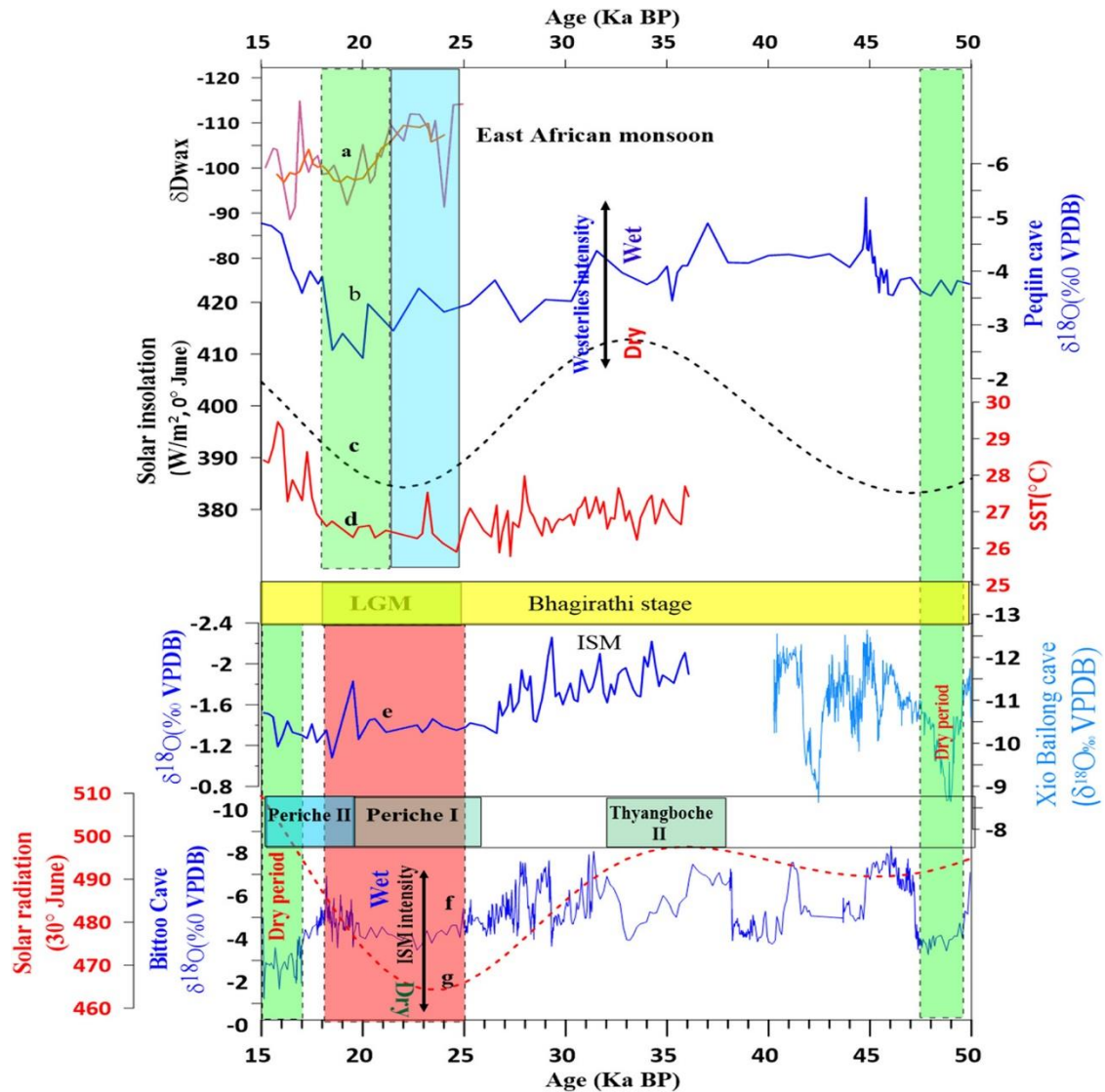
Figure 1. Comparison of different monsoons records over East Africa and Himalaya in the last 50 ka BP. (a) δD leafwax(‰VSMO) records of Tanganyika Lake, East Africa (Tierney et al., 2008); (b) δ18O from Peqiin cave, eastern Mediterranean region (Bar-Matthews et al., 2003); (c) Solar radiation at 0°(w/m2) (Berger and Loutre, 1991); (d) Sea Surface Temperature (SST) from the eastern Indian Ocean (Mohtadi et al., 2014); (e) δ^{18}O (‰ VPDB) reflects ISM intensity; (f) δ^{18}O (‰) from Bittoo cave, Kumaun Himalaya (Kathayat et al., 2016); (g) Solar radiation at 30N (w/m2) (Berger and Loutre, 1991); (i) Xio Bailong cave reflects Asian monsoon intensity (Cai et al., 2006).
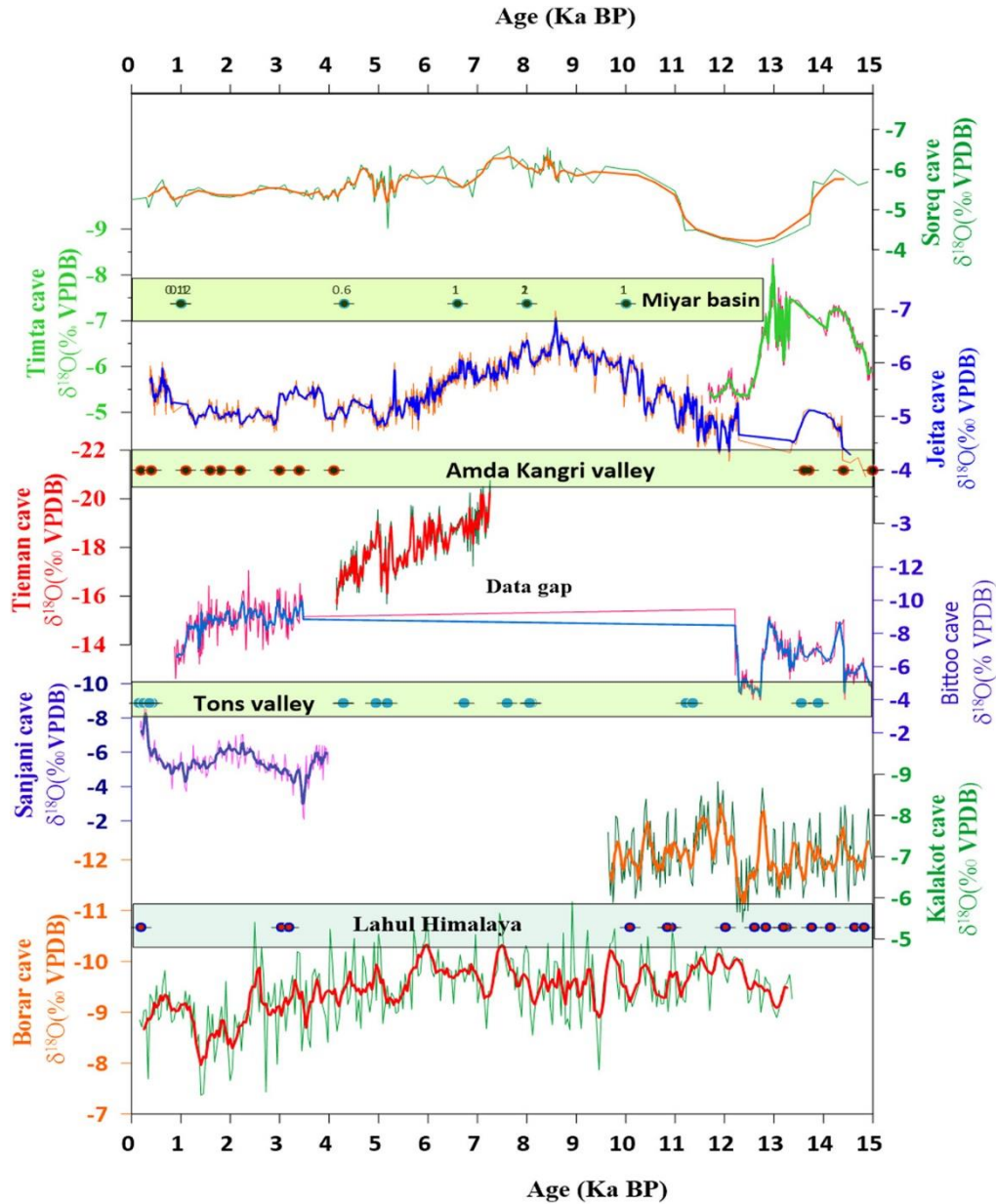
Figure 2. Monsoons variability and glacier variability in different valleys of the Himalaya. the Spleothems δ¹⁸O values are relative to Vienna Pee Dee Belemnite (VPDB). Soreq cave reflects Westerlies precipitation (Bar-Matthews et al., 2003); Miyar basin OSL chronologies (Deswal et al., 2017); Timta cave (Sinha et al., 2005); Jeita cave (Cheng et al., 2015); Amda Kangri glacier (Orr et al., 2018); Tieman cave (Cai et al., 2012); Bittoo cave reflects ISM intensity (Kathayat et al., 2016); Tons valley glacier chronologies; Sanii cave (Kotlia et al., 2015); Kalakot cave (Kotlia et al., 2016); Lahul Himalaya glacier chronologies (Owen et al., 2002); Borar cave (Singh, 2017).

12. 地质、地球物理和板块运动对印度—亚洲碰撞模型和中特提斯的约束

翻译人：周洋 zhouy3@sustech.edu.cn

摘要：在本次研究中，我们将岩石学数据、地幔中板片俯冲形态以及板块运动相结合，用以约束印度—亚洲碰撞模型。为此，我们要了解：（1）西藏三叠纪之后俯冲过程的岩石记录；（2）地幔中俯冲板片的地震层析成像；（3）印度-亚洲大陆碰撞的时间；（4）大印度碰撞前的规模。假设板片垂直下沉至地幔，从地震层析成像可以确定板片位置和几何形状，从而限制古俯冲带的位置和运动方向。整合层析成像和岩石数据，能够约束中特提斯三叠纪之后的俯冲过程。从侏罗纪开始，新特提斯至少受两条俯冲带影响。在 59±1 Ma，印度与亚洲大陆发生碰撞时，在亚洲大陆南部边缘~20°N 的俯冲带开始活跃。此时，在赤道以南位置，另一条俯冲带可能已经活跃，但是从岩石学的角度，却缺乏相应的支持。关于俯冲带的大印度重建包括：（1）最小面积；（2）扩大的面积；（3）大印度盆地重建。我们将这些重建和俯冲带相结合以检验印度—亚洲大陆碰撞的模型。没有可以完全令人满意的单一模型，每个模型都有很多假设，包括对缝合带以及大陆俯冲的局限了解。探索这些挑战对认识印度—亚洲碰撞和陆—陆碰撞具有重要意义。

ABSTRACT: In this study, we integrate bedrock datasets, observations of subducted slabs in the mantle, and plate kinematic constraints to constrain models for the India-Asia collision and the central Tethys oceans. To accomplish this, we review: (1) the post-Triassic bedrock record of subduction in Tibet; (2) seismic tomographic imaging of subducted slabs in the mantle; (3) timing of the India-Asia collision; and (4) the pre-collisional size of Greater India. Following the assumption that slabs sink vertically through the mantle, their positions and geometries determined from seismic tomography constrain the locations and kinematics of paleo-subduction zones.

Integrating this with bedrock constraints allows us to constrain post-Triassic subduction zone confgurations for the central Tethys oceans. Neotethys was consumed by at least two subduction zones since the Jurassic. At the onset of the India-Asia collision at 59 ± 1 Ma, one subduction zone was active along the southern Asian continental margin at ~20°N. At that time, a second may have been active at subequatorial latitudes, but support for this from a bedrock perspective is lacking. This subduction zone confguration allows for three reconstructions for Greater India: The (1) minimum-area; (2) enlarged-area; and (3) Greater India Basin reconstructions. We integrate these reconstructions and subduction zone confgurations in a plate kinematic framework to test their validity for the India-Asia collision. No single model is entirely satisfactory and each invokes assumptions that challenge accepted concepts. These include our understanding of suture zones, and the limits of continental subduction. We explore these challenges and their implications for our understanding of the India-Asia collision and continental collisions in general.
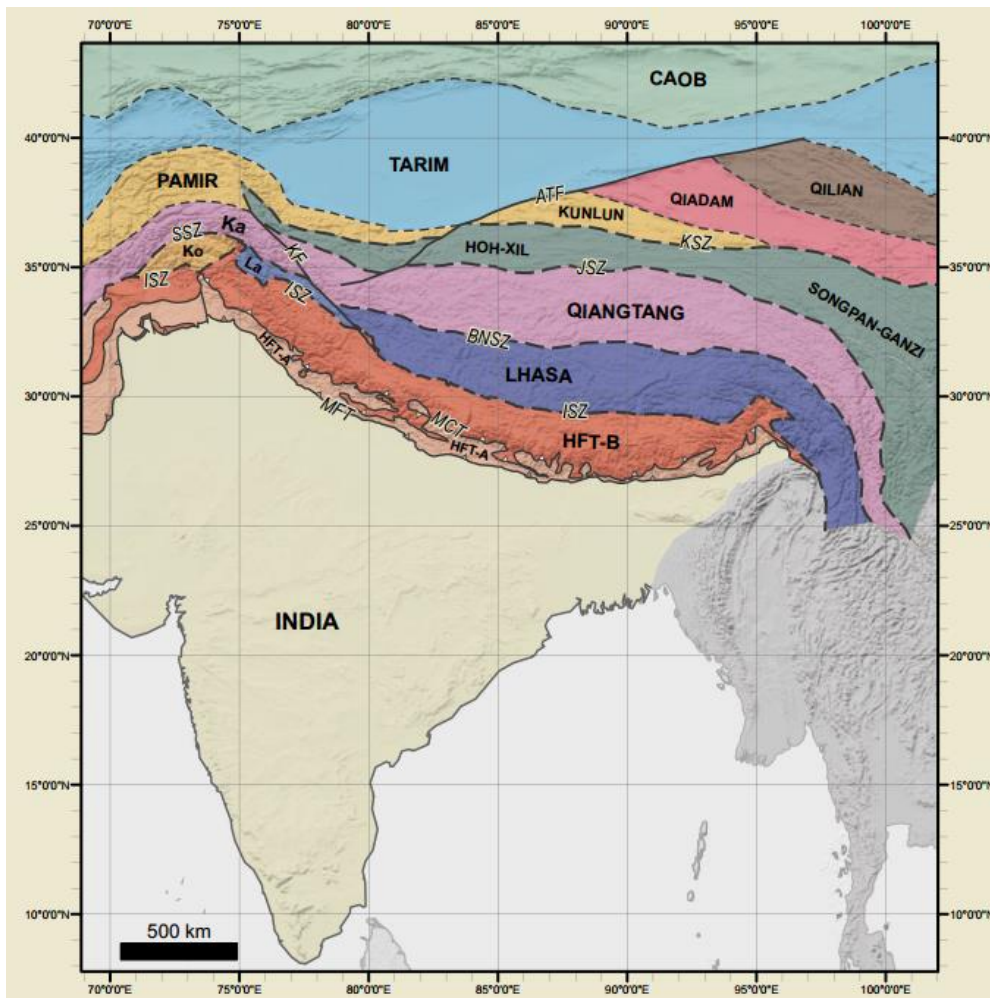

Figure 1. Terrane map of crustal blocks and bounding structures of the Himalaya-Tibet orogenic

system. AFT – Altyn Tagh Fault; BNSZ – Bangong-Nujiang Suture Zone; CAOB – Central Asian Orogenic Belt; HFT-A – Himalaya Fold-and-Thrust Belt, Sequence A (includes Lesser Himalayan Sequence and Subhimalayan Zone; based on Martin, 2017b); HFT-B – Himalaya Fold-and-Thrust Belt, Sequence B (includes Greater Himalayan Sequence and Tethyan Himalayan Sequence; based on Martin, 2017b); ISZ –Indus Suture Zone; JSZ – Jinsha Suture Zone; Ka – Karakoram; KF – Karakoram Fault; Ko – Kohistan; KSZ – Kunlun Suture Zone; La – Ladakh; MFT – Main Frontal Thrust; MCT – Main Central Thrust; SSZ – Shyok Suture Zone. Drawn from Searle et al. (2011), Parsons et al. (2016a), Martin (2017b), Goscombe et al. (2018), Li et al. (2018), and Kapp and DeCelles (2019). Georeferenced overlays (.kml, .kmz) and shapefles of all points, lines, and polygons presented in our map fgures are available for use and editing with global information system software (e.g. Google Earth, GPlates, ArcGIS) in Supplementary Materials 01 and 02.

13. FinIrrSDA:一个磁性形状和分布各向异性的三维模型

翻译人：张伟杰 12031188@mail.sustech.edu.cn

摘要：磁各向异性一般由强磁性颗粒形状各向异性和分布各向异性组成。它们在岩石中的相对重要性取决于许多因素，对此曾有过争议性的讨论。迄今为止，估计其贡献的一个主要挑战是分布各向异性模型针对与在沿直线或平面均匀粒子的分布进行的。由于岩石中的磁铁矿颗粒或孔隙显示出广泛的方向、形状和大小范围，通常排列不规则，需要新的模型来描述分布各向异性，以得到更真实的颗粒和孔隙组合。本研究提出的模型，FinIrrSDA，可以计算不同方向的不平等粒子的形状和分布各向异性的有限不规则组合。模型输出由两个磁化率张量组成:(1)形状各向异性张量; (2)结合形状各向异性和分布各向异性的总张量。FinIrrSDA 可广泛适用于输入数据集，包括已知的合成数据结构，层析数据中的粒子分析，以及在某些假设下的二维图像。该模型有望帮助我们对天然岩石形状和分布各向异性之间相互作用的理解，并有助于进一步解释磁铁矿颗粒所携带的磁性各向异性和磁性孔隙结构。

ABSTRACT: The magnetic anisotropy carried by strongly magnetic particles such as magnetite or ferrofluid-filled pores is generally composed of shape anisotropy and distribution anisotropy. Their relative importance in rocks depends on numerous factors and has been discussed controversially. A major challenge in estimating their contributions so far has been that models for distribution anisotropy only exist for regular arrangements of equal particles along lines or in planes. Because magnetite grains or pores in rocks display wide ranges of orientations, shapes and sizes in generally irregular arrangements, new models are needed to describe distribution anisotropy for more realistic grain and pore assemblies. The model presented in this study, FinIrrSDA, calculates Shape and Distribution Anisotropy for FINite IRRegular assemblies of unequal particles with different orientations. Input parameters are provided as a table with x, y and z coordinates of the particle

centers, and the lengths and orientations of the major, intermediate and minor axes of best-fit ellipsoids. The model output consists of two susceptibility tensors: (1) the shape anisotropy tensor, and (2) the total tensor combining shape and distribution anisotropies. FinIrrSDA can be applied to a wide range of input datasets, including known structures of synthetic samples, particle analyses from tomography data, and, subject to certain assumptions, 2D images. The model will hopefully increase our understanding of the interplay between shape and distribution anisotropies in natural rocks, and facilitate future interpretations of both the magnetic anisotropy carried by magnetite grains, and magnetic pore fabrics.
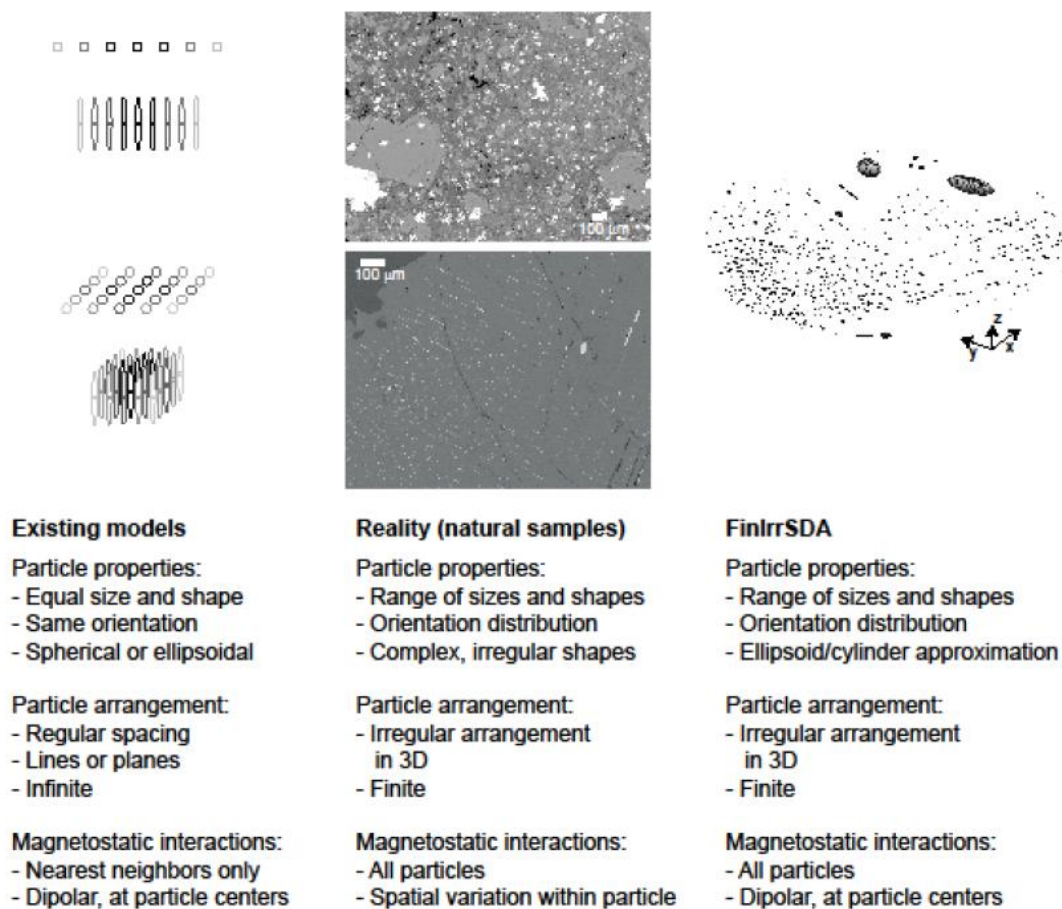

Existing models	Reality (natural samples)	FinIrrSDA
Particle properties:	**Particle properties:**	**Particle properties:**
- Equal size and shape	- Range of sizes and shapes	- Range of sizes and shapes
- Same orientation	- Orientation distribution	- Orientation distribution
- Spherical or ellipsoidal	- Complex, irregular shapes	- Ellipsoid/cylinder approximation
Particle arrangement:	**Particle arrangement:**	**Particle arrangement:**
- Regular spacing	- Irregular arrangement	- Irregular arrangement
- Lines or planes	in 3D	in 3D
- Infinite	- Finite	- Finite
Magnetostatic interactions:	**Magnetostatic interactions:**	**Magnetostatic interactions:**
- Nearest neighbors only	- All particles	- All particles
- Dipolar, at particle centers	- Spatial variation within particle	- Dipolar, at particle centers

Figure 1. Properties of individual particles, their arrangement, and interactions of existing models，compared to typical properties of natural rock samples. Examples for rock samples are backscattered electron images showing a basalt from Cape Verde, and a pyroxene grain in an oxide gabbro from the Duluth Complex, MN, USA. The code FinIrrSDA proposed in this study still relies on approximations with respect to particle shape and the description of magnetic interactions, but closes major gaps between existing models and reality.

14. 由气候异常驱动的罗斯海南极底层水形成

翻译人：张亚南 zhangyn3@mail.sustech.edu.cn

摘要：南极底层水（AABW）是全球翻转环流的下半部分，在年代际到千年尺度上影响深海水体的通风及对热量和碳的保存。AABW 源自南极大陆架，是由强烈的冬季降温和海冰形成造成的水体盐度升高而产生的稠密陆架水，并下沉至深海。AABW 的盐度、密度和体积在过去 50 年间逐渐下降，在罗斯海区域尤为显著，这种变化主要是由于南极冰盖融水的增加。这里，我们通过现场观测罗斯海 AABW 的盐度、密度和水体厚度的恢复情况，结果显示 2018-2019 水体性质与 1990s 观测的结果相似。这次的恢复主要是由于陆架海冰增加的影响，2015-2018 年间 positive Southern Annular Mode 和极端厄尔尼诺现象的不寻常的结合引发了异常风强迫，从而导致海冰形成的增加。我们的研究强调了 AABW 形成对远程强迫的敏感性 ，并表明气候异常可以驱动局部海冰暂时的增加，从而从而抵消冰盖融水减弱 AABW 形成的影响。

ABSTRACT: Antarctic Bottom Water (AABW) supplies the lower limb of the global overturning circulation, ventilates the abyssal ocean and sequesters heat and carbon on multidecadal to millennial timescales. AABW originates on the Antarctic continental shelf, where strong winter cooling and brine released during sea ice formation produce Dense Shelf Water, which sinks to the deep ocean. The salinity, density and volume of AABW have decreased over the last 50 years, with the most marked changes observed in the Ross Sea. These changes have been attributed to increased melting of the Antarctic Ice Sheet. Here we use in situ observations to document a recovery in the salinity, density and thickness (that is, depth range) of AABW formed in the Ross Sea, with properties in 2018–2019 similar to those observed in the 1990s. The recovery was caused by increased sea ice formation on the continental shelf. Increased sea ice formation was triggered by anomalous wind forcing associated with the unusual combination of positive Southern Annular

Mode and extreme El Niño conditions between 2015 and 2018. Our study highlights the sensitivity of AABW formation to remote forcing and shows that climate anomalies can drive episodic increases in local sea ice formation that counter the tendency for increased ice-sheet melt to reduce AABW formation.
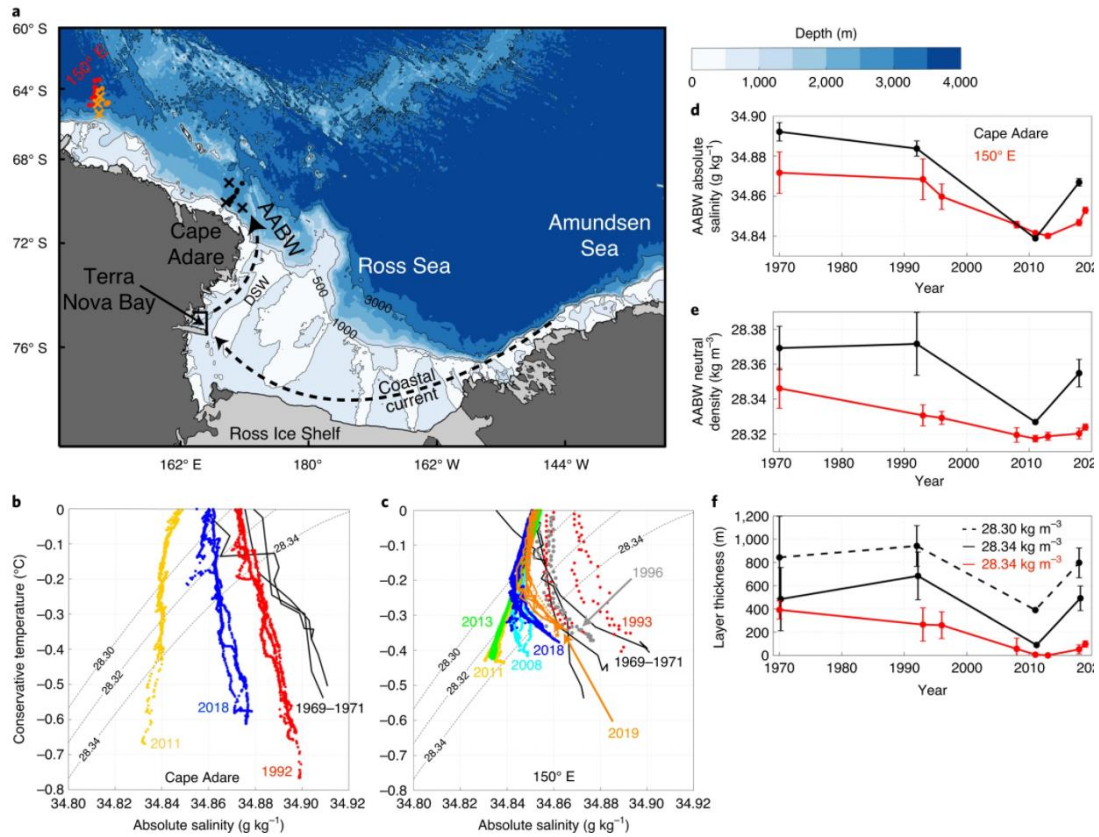

Figure 1. Recovery of AABW formed in the Ross Sea. **a**, Map of the study area with bathymetry overlaid. Red (black) circles denote observations collected at 150° E (Cape Adare) during repeated transects between the early 1990s and 2018. Orange (black) crosses indicate observations collected at 150° E (Cape Adare) during the Eltanin and Thomas Washington expeditions in 1969–1971, while orange circles denote data collected by a deep float in 2019 (Methods). **b,c**, Conservative temperature versus absolute salinity at Cape Adare (**b**) and at 150° E (**c**; see location in a). Overlaid are the 28.30, 28.32 and 28.34 kg·m⁻³ neutral-density surfaces for reference. d,e, Average AABW absolute salinity (**d**) and neutral density (**e**). AABW is defined18 as water denser than 28.30 kg·m⁻³. **f**, Thickness of the 28.30- and 28.34-kg·m⁻³ layers at Cape Adare (black) and thickness of the 28.34-kg·m⁻³ layer at 150° E (red). Thickness is calculated between the depth of the density surface and the seafloor. Means (circles) and standard deviations (vertical bars) are calculated using observations collected each year along the two transects. Observations from the Eltanin and Thomas Washington expeditions are temporally averaged between 1969 and 1971.
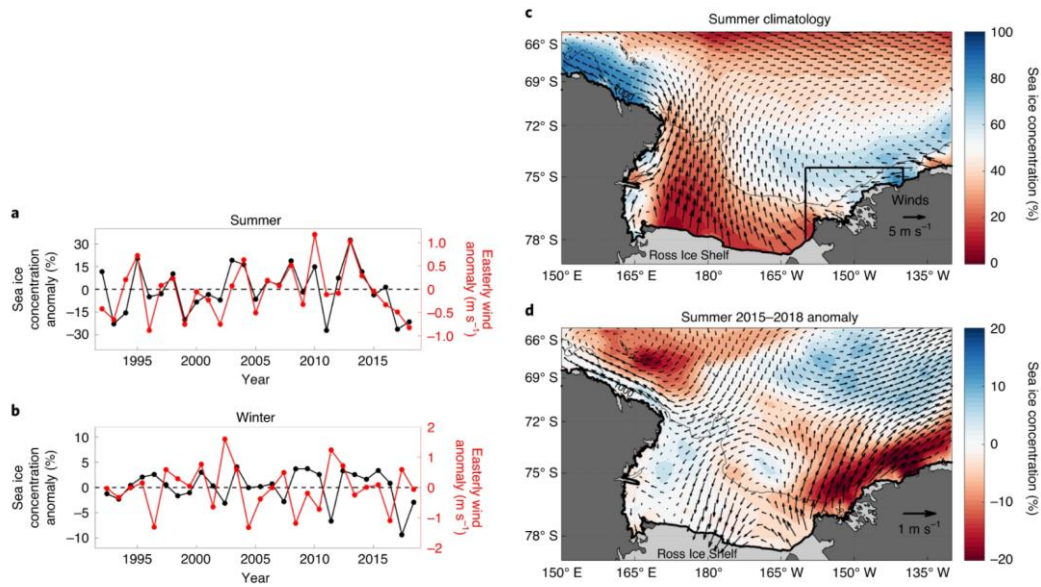
Figure 2. Interannual variability of winds and sea ice in the western Amundsen Sea. **a**, Summer (November to February) anomalies of easterly winds and sea ice concentration in the western Amundsen Sea between 1992 and 2018 (Methods). Values are obtained from a spatial average inside the black box in **c**. The south–north transect on the western side of the box represents the gate used to estimate the sea ice inflow from the Amundsen to the Ross Sea. Easterly winds are obtained by rotating the coordinate system anticlockwise by 30° to follow the coastline. **b**, Same as a for winter (March to October). **c**, **d**, Summer climatology (**c**) and 2015–2018 anomaly (**d**) of winds and sea ice concentration in the Ross and western Amundsen seas. The 1,000-m isobath is shown in c and d to visualize the margin of the continental shelf.
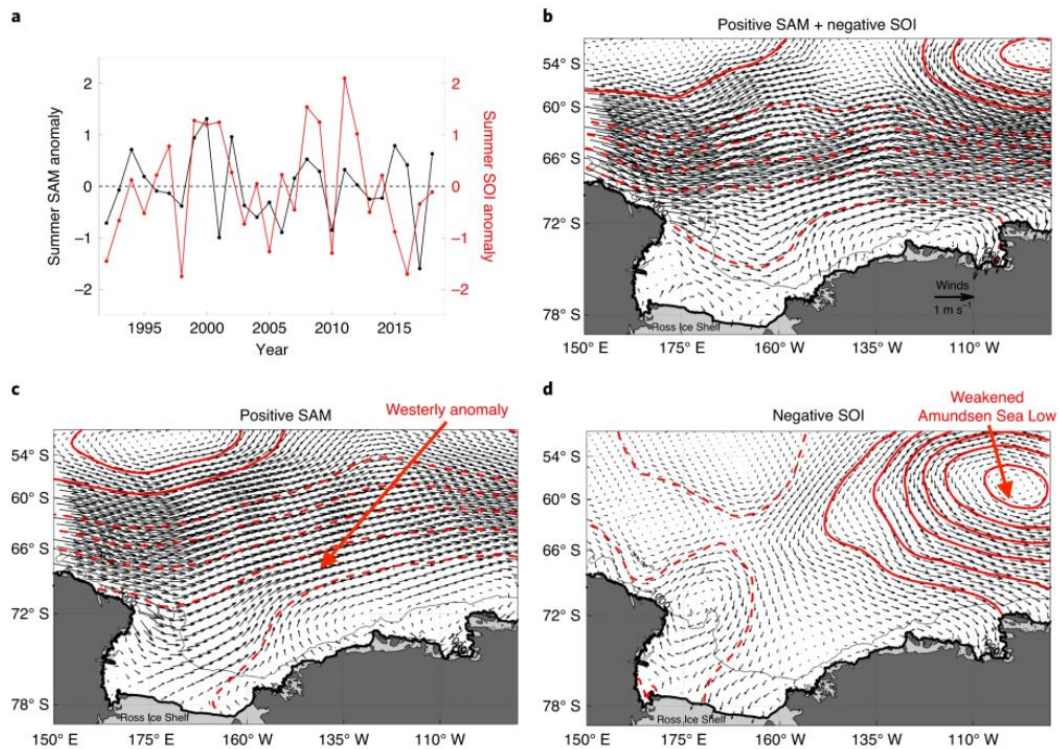

Figure 3. Anomalous climate forcing between 2015 and 2018. **a**, Summer anomalies of SAM and

SOI between 1992 and 2018. The 2015–2018 period is characterized by positive SAM and negative SOI. **b**, Multiple regression (Methods) of SAM and SOI onto mean sea-level pressure (mbar, red lines), and associated winds. Contours of mean sea-level pressure are every 0.5 mbar. Solid (dashed) lines mean positive (negative) anomalies. **c**, The SAM component of the regression. This panel highlights atmospheric variability associated with positive SAM. **d**, The same as **c**, for (negative) SOI. In this panel contours are every 0.25 mbar. Note how both positive SAM and negative SOI cause westerly anomalies over the Amundsen Sea. The 1,000m isobath is shown in **b–d**.
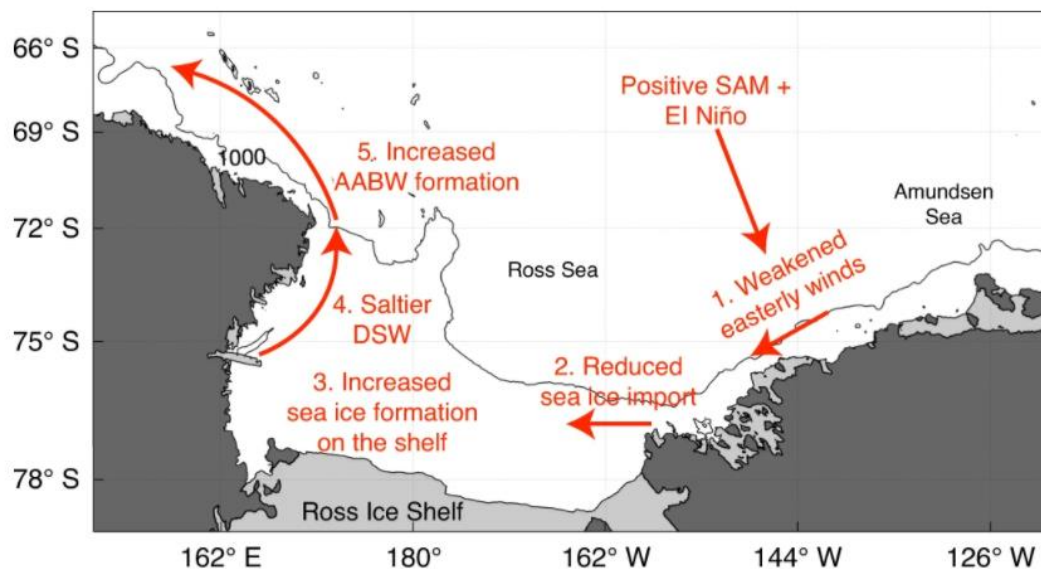

Figure 4. Schematic illustrating the physical mechanisms driving enhanced AABW formation in the Ross Sea. The unusual combination of positive SAM and El Niño resulted in weaker easterly winds in the western Amundsen Sea, less import of sea ice and a more open sea ice pack with higher rates of sea ice formation on the Ross Sea continental shelf. The resulting increase in DSW salinity enhanced the formation of AABW. The 1,000-m isobath is highlighted to visualize the margin of the continental shelf.